Characteristics of tropical Squall-lines over Venezuela

By
Ralph W. Grover

Department of Atmospheric Science
Colorado State University
Fort Collins, Colorado

This research was supported by the NSF, Atmospheric Sciences Section,
under Grant GA-33182.
Principal investigator: A.K. Betts
July 1974

Department of
Atmospheric Science

Paper No. 228

CHARACTERISTICS OF TROPICAL SQUALL-LINES OVER VENEZUELA

by

Ralph W. Grover

This research was supported by the National Science Foundation,
Atmospheric Sciences Section, under Grant GA-33182
Principal Investigator: A. K. Betts

Department of Atmospheric Science
Colorado State University
Fort Collins, Colorado
80523

July 1974

Atmospheric Science Paper Number 228

ABSTRACT

CHARACTERISTICS OF TROPICAL SQUALL-LINES
OVER VENEZUELA

The characteristics of fifteen mesoscale storm systems observed during the 1972 Venezuelan International Meteorological and Hydrological Experiment were compared with the predictions of a dynamic cumulonimbus and squall-line model proposed by Moncrieff (1974a). The fifteen systems seemed to fall into three groups: one group of six were land tropical squall-lines; a second group of seven are simply called non-squall-lines; and the third group of two storms formed a distinct class which are here called large non-propagating mesosystems. Moncrieff's theoretical model, which predicts storm propagation speeds, is applied to each group, and closest agreement is found with the group of squall- lines. A simple composite of the inflow and outflow environments of the squall-lines is presented. This shows the complete dynamic and thermodynamic transformation of the atmosphere, which, as predicted by the theory, results from the passage of a squall-line. A schematic model for a squall-line is presented from this composite. It suggests that although the observed updraft configuration may be similar to that of the theoretical model, the observed downdraft is more complex.

ACKNOWLEDGEMENTS

This research was supported by the Atmospheric Sciences Section of the National Science Foundation under Grant GA-33182. The VIMHEX II field experiment was additionally supported by the office of Naval Research under Contract No. 014-68A-0493-002, the Facilities Laboratory of the National Center for Atmospheric Research, and the Meteorological Service of the Venezuelan Air Force.

This paper comprises a thesis accepted in partial fulfillment of the requirements of an M.S. degree at Colorado State University. The author wishes to express his sincere appreciation to his advisor, Dr. A. K. Betts, and to Dr. M. W. Moncrieff for their advice and encouragement; and to Professor L. O. Grant and Dr. W. Z. Sadeh for their guidance during the graduate program.

Additional thanks are due to Mrs. Susan Kuehl, Mrs. Brenda Beattie, Mrs. Polly Martin and Mr. Richard Miller for their invaluable assistance in the typing of the manuscript, data reduction and computer programming.

Special appreciation is expressed to the author's wife, Cynthia, for her patience and encouragement.

TITLE:

CHARACTERISTICS OF TROPICAL SQUALL-LINES OVER VENEZUELA

TABLE OF CONTENTS

TABLE OF CONTENTS - Continued

LIST OF TABLES

LIST OF FIGURES

LIST OF FIGURES – Continued

LIST OF SYMBOLS

T	temperature
θ	potential temperature
θ_e	equivalent potential temperature
θ_{es}	saturation equivalent potential temperature
R_d	gas constant of dry air
c_y	specific heat at constant volume
c_p	specific heat at constant pressure
p	pressure
δ_p	perturbation pressure
ρ	density
ρ_0	density of basic state
g	gravity
x	horizontal coordinate
y	horizontal coordinate
z	vertical coordinate
z_o	height of inflow streamline
z_{o_*}	inflow level for parcel θ_e
$\vec{k}$	unit vector in positive z direction
$\vec{v}$	velocity vector
U	velocity magnitude
L	length scale
u_a	u component of velocity parallel to storm motion
u_r	u component of velocity relative to storm coordinates
U_M	relative inflow velocity at $z = 0$
c	predicted propagation speed

C_o	observed propagation speed
ϕ	log-potential temperature
ϕ_o	environmental log-potential temperature
ϕ_p	parcel log-potential temperature
ϕ^*	ϕ_p for $z_o = \mathbf{z_{o_*}}$
δ_ϕ	$\phi_p - \phi_o$
ψ	stream function
μ	kinematic viscosity
Ri	Richardson Number
Re	Reynolds Number
Ro	Rossby Number
$\bar{\theta}_e$	averaged θ_e of parcel for observed storms
α	α (Ri)
χ	entrainment factor
S_E	$\Delta p \chi$
(P)	denotes parcel quantity
(E)	denotes environmental quantity

1. INTRODUCTION

1.1 General

A number of recent studies (Betts, 1970, 1973 a, b; Moncrieff and Green, 1972; Arakawa and Schubert, 1974) have contributed to further understanding of the relationships between cumulus convection and the larger scale motions. Although these relationships are not completely understood, they are known to be of particular importance in the tropics. Malkus and Riehl (1964) suggested the existance of controls on cloud organization and precipitation by the large-scale motions. The JOC Study Group on Tropical Disturbances (1968) presented documented evidence of organization of maritime tropical clouds into "cloud clusters". Although the importance of explaining this organization of convective elements into clusters and the cluster's relationship to the tropical wave cannot be minimized, the structure of the convective elements within the cluster and their relationship to the general flow are fundamental to the understanding of atmospheric interactions.

In an effort to achieve an understanding to these interactions, several recent tropical field experiments, including BOMEX (Barbados Oceanographic and Meteorological Experiment), ATEX (Atlantic Trade Wind Experiment), VIMHEX I and II (the First and Second Venezuelan International Meteorological and Hydrological Experiments) and GATE (GARP Atlantic Tropical Experiment) have been conducted. The impetus for these experiments has been the need for the collection of more sophisticated observational data on the cumulus, cumulonimbus and synoptic scales than is currently available through satellite or standard weather service observations. The results obtained from this data are providing numerical modelers with much needed feedback.

The purpose of the research presented here is to provide modelers of tropical cumulonimbus convection with information on the behavior and dynamic structure of land tropical squall-lines observed during the Second Venezuelan International Meteorological and Hydrological Experiment. The objectives of this paper are: 1) to evaluate a recently proposed tropical cumulonimbus and squall-line model developed by M. W. Moncrieff (1974 a) by comparing the predictions of the model against the observed tropical squall-lines, and 2) to construct an observational model of a land tropical squall-line from the storm systems studied.

1.2 VIcMHEX II

VIMHEX II was conducted from June to September, 1972. The field headquarters were located at Carrizal, Venezuela (9°22.8'N and 66°55.0'W), in the north central section of the country approximately 150 km south- southwest of Caracas, Venezuela. Located at the field site were a GMD-1 radiosonde unit and a modified 10 cm M-33 radar with a 2° beam width and return signal attenuation capabilities.

The radiosonde soundings were the principle means of measuring the state of the atmosphere. For this, the new VIZ-National Weather Service 1290 series radiosonde was used. Riehl and Betts (1972) and Betts et al. (1974) have shown this new instrument has overcome the systematic humidity errors found to exist in the old model radiosondes used in BOMEX, ATEX and VIMHEX I. The 327 soundings launched during the course of the experiment fell into three categories:

1. Routine soundings made on a twice-daily basis.
2. Soundings made prior to the onset of the cumulonimbus convection, during and after the convection had passed.

3. Special soundings taken on several days when the convection was suppressed.

Of particular interest to this research is the sequence of soundings that measured the atmosphere prior to, during and after cumulonimbus convection. To reduce the launch delay caused by the calibration of the radiosondes during cumulonimbus activity, precalibrated radiosondes were used (Betts, 1973 c). This allowed as many as six radiosondes, depending on the size and duration of the cumulonimbus convection, to be launched as frequently as one every seventy-five minutes.

The radar system consisted of an observer and camera scope system set at a horizontal range of 90 km. At the first sign of cumulonimbus convection the camera scope was activated and for the duration of the convective activity, the following procedure was conducted at fifteen minute intervals.

The antenna sweep began at a 2˚ elevation angle and was incremented at 2˚ steps through 20˚, where the step was increased to a 4˚ interval. This sequence was terminated when either the convective tops were surpassed or 60˚ was reached. Once the data was returned to Colorado State University, the 35 mm film from the camera scope was projected on a microfilm reader at a scale of one centimeter equalling ten kilometers. By tracing the individual echo perimeters at 2˚ and zero return attenuation at each fifteen minute interval a composite of the storm system as it moved across the field of observation was obtained. A sample composite of a storm system is presented in Figures 1.1.

1.3 Storm System Selection

Storm systems were initially selected to evaluate Moncrieff's dynamic model of tropical cumulonimbus and squall-lines. The two basic assumptions of the theory are: (i) that if one moves with the convective system, the relative flow field is steady, and (ii) that the flow remote from the system is two-dimensional in the x, z plane, where x is parallel to the motion of the system. The latter assumption implies the idealized system is infinite in y, where the y axis of this storm is normal to the direction of the mean flow. No cloud system in nature will meet these assumptions; therefore, it was necessary to relax them. The following criteria were established for selecting observed storm systems from VIMHEX II. First, the storm systems selected were to have a major axis length (y-axis) greater than the minor axis length (x-axis). Second, the major axes of these storm systems were to be perpendicular to the mean flow. Finally, to approximate a steady state system, their echo composites at 2° must show very little change of shape, particularly during measurement of the inflow regions. The last qualification will be discussed in Chapters 2 and 3.

This method of selection resulted in fifteen storm systems being chosen for study. Presented in Table 1.1 are the fifteen storms, their radiosondes and observed storm statistics. A sample radar composite of a selected storm system is presented in Figure 1.1. This storm (number 47) is quite large (maximum area equaled 2554 km). Its major axis length =80 km is a minor axis length of ≈25 km.

TABLE 1.1

Selected Storm Systems

STORM NUMBER	RADIOSONDE NUMBER	DATE MONTH/DAY		MAXIMUM AREA KM^2	MAXIMUM HEIGHT KM	DIRECTION N = 0 /SPEED MS^{-1}
16	87	June	30	1287	13.3	094/16.1
17	88		30	980	13.8	084/11.8
27	99	July	3	2393	12.0	082/11.3
	100					
35	120		9	3290	15.6	086/9.1
126	164		22	2670	10.9	091/2.8
47	176		24	3677	9.9	065/13.4
53	191		28	2851	15.5	107/11.4
	192					
60	226	August	7	1471	9.5	095/12.5
	227					
134	235		9	2380	13.1	094/5.4
	236					
64	241		11	2354	14.8	089/18.3
68	245		12	696	15.5	104/13.2
80	271		20	909	14.0	091/10.8
91	288		25	1690	14.9	067/9.4
	289					
108	312	September	1	4767	16.2	095/5.2
109	316		2	11481	14.1	087/3.1

1.1 Composite radar echo of squall-line number 47 July 24, 1972.

All fifteen storms had a major axis length two to five times longer than the minor axis length. The mean wind of the lower troposphere for all storm systems was generally easterly, varying almost ~45 degrees from 090°. As was the case with Storm 47, all the selected storm system's major axes were approximately normal to the mean flow of the lower troposphere. From Figures 1.1 it is seen that as Storm 47 approached the radar/radiosonde site (located at the scope's center) its shape was relatively unchanging. Thus, it was assumed that no major dynamic changes were occurring within the storm. The assumption of steady state was the least rigorously applied criterion in the selection of the fifteen storms. It is important to note that although Storm 47 appears as a solid echo at two degrees with no signal alteration, the storm system as an entity was comprised of numerous active single cells, as was the case for the remaining fourteen storm systems.

For Moncrieff's cumulonimbus and squall-line model to be properly evaluated, the storm systems themselves were thoroughly analyzed from an observational standpoint. During this analysis their propagation speeds were studied, their geiometric and dynamic characteristics, and the synoptic conditions existing at the time of the storm's occurrence and the structural changes of the atmosphere that occurred as a result of the storm's passage.

As a result of this analysis, three separate and distinct groups of storms emerged from the original fifteen storms. Group 1 storms (27, 35, 47, 60, 64 and 91) were identified as squall-lines. Group 2 storms (16, 17, 126, 53, 134- 68 and 80) will be referred to as "non-squall-lines." Group 3 storms (108 and 109) are, because of their singular uniqueness, referred to as "large, non-propagating mesosystems". All three groups, it must be remembered, may be distinctly different from the remainder of

the VIMHEX II storm systems. In particular, they are all systems with some mesoscale structure rather than isolated single cell cumulonimbus.

To summarize the characteristics of the squall-line, non-squall-line and non-propagating mesosystem, Table 1.2 has been prepared from the results of Chapter 4. Included in this table are the results of computing the Richardson Number (see Chapter 2 and 3) from the inflow environment of the storm.

Table 1.2

Storm Grouping Criteria

	Squall-line (Group 1)	Non-squall-line (Group 2)	Mesosystem (Group 3)
Richardson No.	Ri≤-0.93	Ri≤-0.91	--
Inflow into front of storm at all levels	yes	no	no
Synoptic feature 850 mb trough	yes	no	yes
Definite line configuration	yes	no	no
Correlated predicted vs observed propagation speeds	yes	no	no
Strong modification of the atmosphere	yes	no	undetermined

Chapter 4 discusses in detail the analysis of the specific group characteristics mentioned in Table 2.1. In addition, based upon a composite of inflow and outflow soundings of the six squall-lines, an observational model is presented.

In Chapter 2, a brief discussion of Moncrieff's model is presented. The assumptions and definitions as well as the theory of the model are discussed.

In Chapter 3, a description of the method used for calculating the available potential energy, available kinetic energy and the Richardson Number is presented. Methods used to determine certain observed storm parameters are discussed. Included in this chapter are the results of testing Moncrieff's method of choosing cloud base and cloud top for the model. A discussion of potential errors in the Richardson Number concludes this chapter.

2. THEORY

2.1 General

The cumulonimbus model proposed by Moncrieff (1974 a) predicts the structure of a "tropical cumulonimbus and squall-1ine" as a function of the large scale flow. Moncrieff (1974 a) shows that the Richardson Number for the tropical cumulonimbus or squall-line can be calculated from the undisturbed large scale flow in front of a moving convective system, the propagation speed of the cumulonimbus is a function of the Richardson Number, and the outflow velocity profile of the cumulonimbus can be predicted from the inflow velocity profile.

2.2 Model Assumptions and Definitions

The model treats the atmosphere as inviscid. A comparison of the acceleration term $D\vec{v}/Dt$ with the viscous force term $\mu \nabla^2 \vec{v}$ (per unit mass) in the momentum equation shows that the viscous forces are negligible if the Reynolds Number ($Re = UL/\mu$) for the flow is much greater than one.

$$\frac{D\vec{v}}{Dt} : \mu \nabla^2 \vec{v}$$

$$u \frac{\partial u}{\partial x} : \mu \nabla^2 u$$

$$\frac{U\,U}{L} \Big/ \frac{\mu\,U}{L}$$

where $\mu \simeq 1.5 \times 10^{-5}$ m^2 s^{-1} for atmospheric ranges. For the molecular viscosity to warrant consideration, L would need to approach 1 mm for U = 10 ms^{-1}. For a scale of motion where L = 10 km, this term may be neglected. Turbulence within the cumulonimbus is neglected by defining a mean streamline through the system.

Next, the model neglects the earth's rotation. Comparing Du/Dt with fv shows this as a valid assumption.

$$\frac{Du}{Dt} : fv$$

$$u\,\frac{\partial u}{\partial x} : fu$$

$$\frac{U\,U}{L} : fU$$

where the ratio of these two terms defines the Rossby Number Ro = U/fL. The effect of the earth's rotation on a motion system cannot be neglected if the parcel stays within the tropical system for longer than $\frac{L}{U} \sim f^{-1} \sim$ 11 hours. If for a cumulonimbus L = 10 km and U = 10 ms^{-1}, then $\frac{L}{U} \simeq$ 0.28 hours.

An important assumption relevant to the idealized cumulonimbus is that it be a steady state system. Steady is to be interpreted as the form of the storm remaining unchanged with time, although its position relative to the earth may change (Moncrieff and Green, 1972). The coordinate axes are chosen to move with the propagation speed (c) of the storm so that relative to these axes the wind field is stationary. Finally, the motion field of the cumulonimbus is two dimensional in x and z. Relative to the cumulonimbus, x is positive in the direction of the atmospheric flow, y is positive to the left of this motion and z is positive upwards.

The schematic flow field for the idealized tropical cumulonimbus and squall-line is presented in Figures 2.1. The remote flow is assumed two dimensional but within the cumulonimbus the flow must be three dimensional. However, when the flow is considered steady, streamlines may be fol1 owed through the cumulonimbus from inflow to outflow without

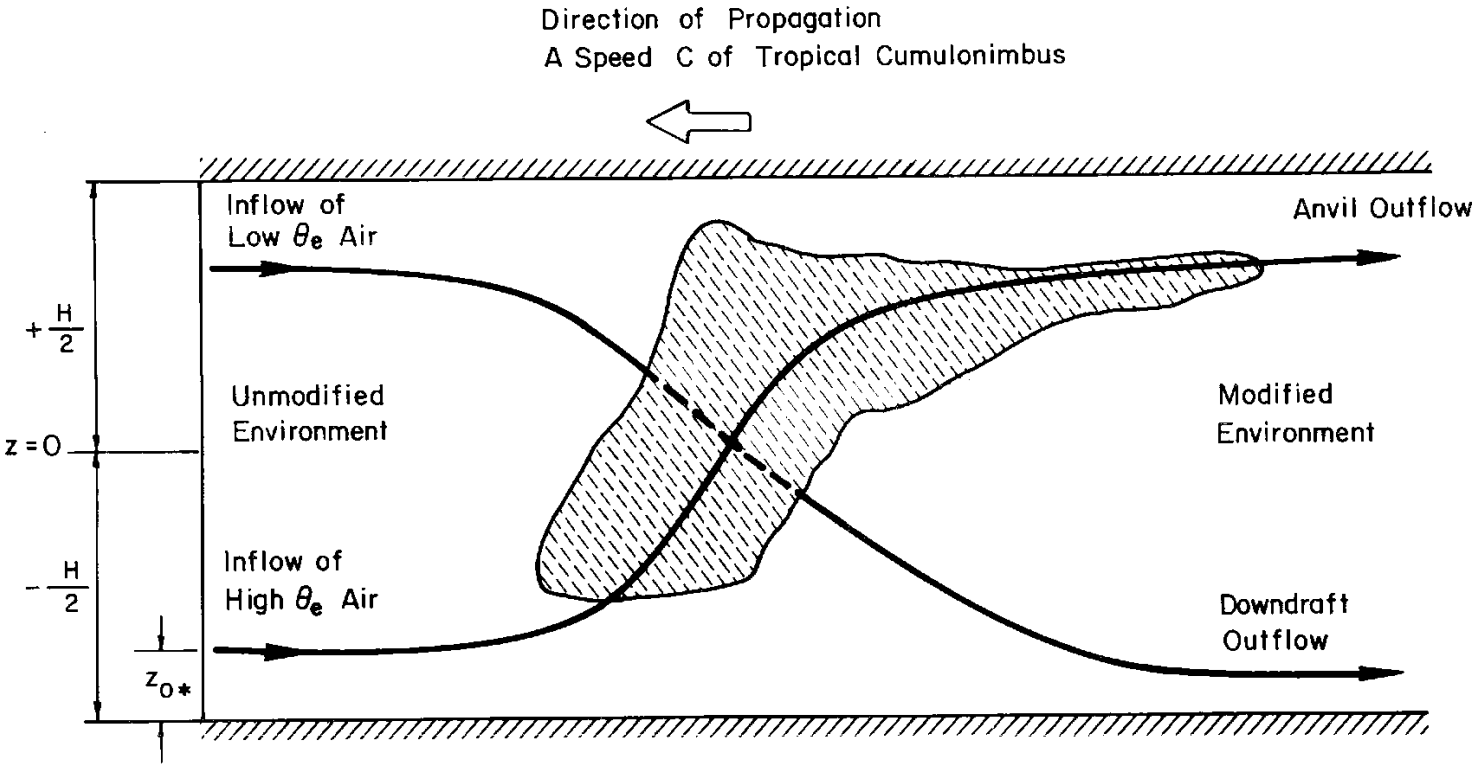

Figure 2.1 - Schematic diagram of relative flow for tropical cumulonimbus (after Moncrieff, 1974a).

the necessity of explicitly specifying the parcel path within the cumulonimbus (the three dimensional region). The motion within the cumulonimbus is stipulated as being moist adiabatic. An important requirement of the model that can be visualized with the aid of Figure 2.1 is there must be inflow into the front of the system at all levels.

2.3 Theoretical Formulation

The atmospheric far from the idealized cumulonimbus is hydrostatic with constant static stability, $B = d(\phi_0)/dt$. For Boussinesq flow, the momentum equation in relative coordinates is then

$$\frac{D\vec{v}}{Dt} + \nabla\left(\frac{\delta p}{\rho o}\right) - g\delta\phi\vec{k} = 0 \qquad 2.1$$

where δp and $\delta\phi$ are the deviations of pressure and log-potential temperature $[\phi = \ln\theta = (cv/cp)\ln(p/p_o) - \ln(p/p_0)]$ from there values in the hydrostatic reference atmosphere which is taken as the remote inflow and K is a unit vector in the direction of increasing z. Eq. 2.1 can be integrated exactly (Moncrieff and Green, 1972) to give a quantity which is conserved along a streamline in stream function (ψ) coordinates $[\phi(x,z) = \phi(\psi, z - z_o)]$

$$\frac{1}{2}\vec{v}_1^{\,2} + \left(\frac{\delta p}{\rho_0}\right)_1 - \int_{z_0}^{z} g\delta\phi_p dz = \frac{1}{2}\vec{v}_0^{\,2} \qquad 2.2$$

where Moncrieff has stipulated that $\delta\phi_p = \phi_p - \phi_0$ (p denotes parcel).

Eq. 22 is a generalization of Bernsulli's equation for compressible Boussinesq flow. The subscript (1) denotes outflow and (o) denotes inflow for a system traveling from east to west. Since the remote flow is horizontal it must be hydrostatic so that

$$\frac{\partial}{\partial z}\left(\frac{\delta p}{\rho_0}\right)_1 = g\delta\phi_1 \text{ as } x \rightarrow +\infty \qquad 2.3$$

Now mass conservation in the Boussinesq form is

$$\text{div}(\rho_0\vec{v}) = o \qquad 2.4$$

or when integrated over the volume of a stream tube in relative coordinates is

$$\rho_0\vec{V}_0 dS_0 = \rho_1\vec{v}_1 dS_1 \qquad 2.5$$

where dS_o and dS_1 are elemental cross-sectional areas of a stream tube,

Combining Eqs. 2.2, 2.3 and 2.5 give

$$\left(\frac{\rho_0 dz_0}{\rho_1 dz_1}\right)^2 = 1 - \frac{\Delta p}{\frac{1}{2}\rho_0\vec{v}_0^{\,2}} + \frac{1}{\frac{1}{2}\vec{v}_0^{\,2}}\left[\int_z^{z_1} g\delta\phi_p dz - \int_0^{z_1} g\delta\phi_1 dz\right] \qquad 2.6$$

The parcel is assumed to follow a saturation pseudo-adiabatic, or

$$\frac{D\phi_p}{Dt} \simeq w\Gamma_s \qquad 2.7$$

where Γ_s is the saturated pseudo-adiabatic lapse rate.

Equations 2.6 and 2.7 are soluble for the out flow velocity profile in terms of the inflow velocity profile (v) and the propagation speed (c), where the relative inflow velocity equals the absolute velocity minus the propagation speed. For complete theoretical development see Moncrieff and Green (1972), and Moncrieff (1972, 1973 and 1974a).

Moncrieff (1974a) defines a Richardson Number for the general case as the ratio of the available potential energy to the available kinetic energy or

$$\mathrm{Ri} = \frac{\mathrm{APE}}{\mathrm{AKE}} = \frac{\int_{z_0}^{z_1} g(\phi_p - \phi_0)\mathrm{d}z}{\frac{1}{2}\left[\int_{z_0}^{z_1} \frac{\partial u}{\partial} r_0 \mathrm{d}z\right]^2} \qquad 2.8$$

where the denominator of Eq. 2.8 is a measure of the inflow available kinetic energy. For the computational procedure used in calculating the Richardson Number see Chapter 3.

In Eq. 2.8 ϕ_0 is a measure of the log-potential temperature far in front of the storm. ϕ_0 is determined from radiosonde measurements made prior to the onset of convection.

The evaluation of ϕ_p is not as straightforward as ϕ_0. ϕ_p is dependent on the parcel under consideration and the level (z_0) at which the moist adiabatic ascent begins. This implies a unique equivalent potential temperature (θ_e) associated with each parcel. Moncrieff (1974a) considers the entire boundary layer (surface to 900 mb) as being processed by the cumulonimbus and transported to the high troposphere. Consequently, a characteristic inflow height is chosen at the middle of the planetary boundary layer or $z_0 = z_{0^*} \simeq ½$ km; and the outflow height, z_1, approximately equals H, the equilibrium level for the parcel. Therefore, a measure of the amount of available potential energy for the cumulonimbus is

$$\mathrm{APE} = \int_{z_{0*}}^{H} g(\phi_* - \phi_0)\mathrm{d}z \qquad 2.9$$

where ϕ_* is the value corresponding to the saturated pseudo-adiabatic parcel ascent from $z_0 - z_{0^*}$. The available potential energy defined in Eq. 2.9 is equal to the positive area on a thermodynamic diagram. The calculation of the available kinetic energy is also conducted between the limits of z_{0^*} and H.

2.4 Propagation Speed

Predicting the propagation speed of a cumulonimbus is a fundamental problem dealt with by the theory. For an undisturbed velocity profile of the form $u_{r_0}(z) = A|z_0| + u_M$ (Figure 2.3) where u_M is the undisturbed relative inflow velocity at z = 0 and A is a constant, the propagation speed, c, or in nondimensional form $c - u_M/(APE)^{1/2}$, has been found as a function of Ri (Moncrieff, 1974a).

Figure 2.2 shows c as a function of Ri for

$$c = u_M + \alpha(APE)^{1/2}$$

where $\alpha = \alpha(Ri)$. For Richardson Numbers in the range of the selected storms see section 4.2. Section 4.5 shows the results of the observed propagation speed compared with that predicted by theory for the fifteen storms.

2.5 Velocity Profiles

The theory requires that there be inflow into the system at all levels. This is illustrated by Figure 2.1. At the low levels, there is inflow of high θ_e air that rises through the cumulonimbus and exits through the anvil at the rear. At high levels in front of the cumulonimbus, low θ_e air enters the system, "descends" and exits near the surface behind the system. This configuration of the updraft is satisfactory. However, the downdraft as shown in Figure 2.1 is not realistic in two dimensions.

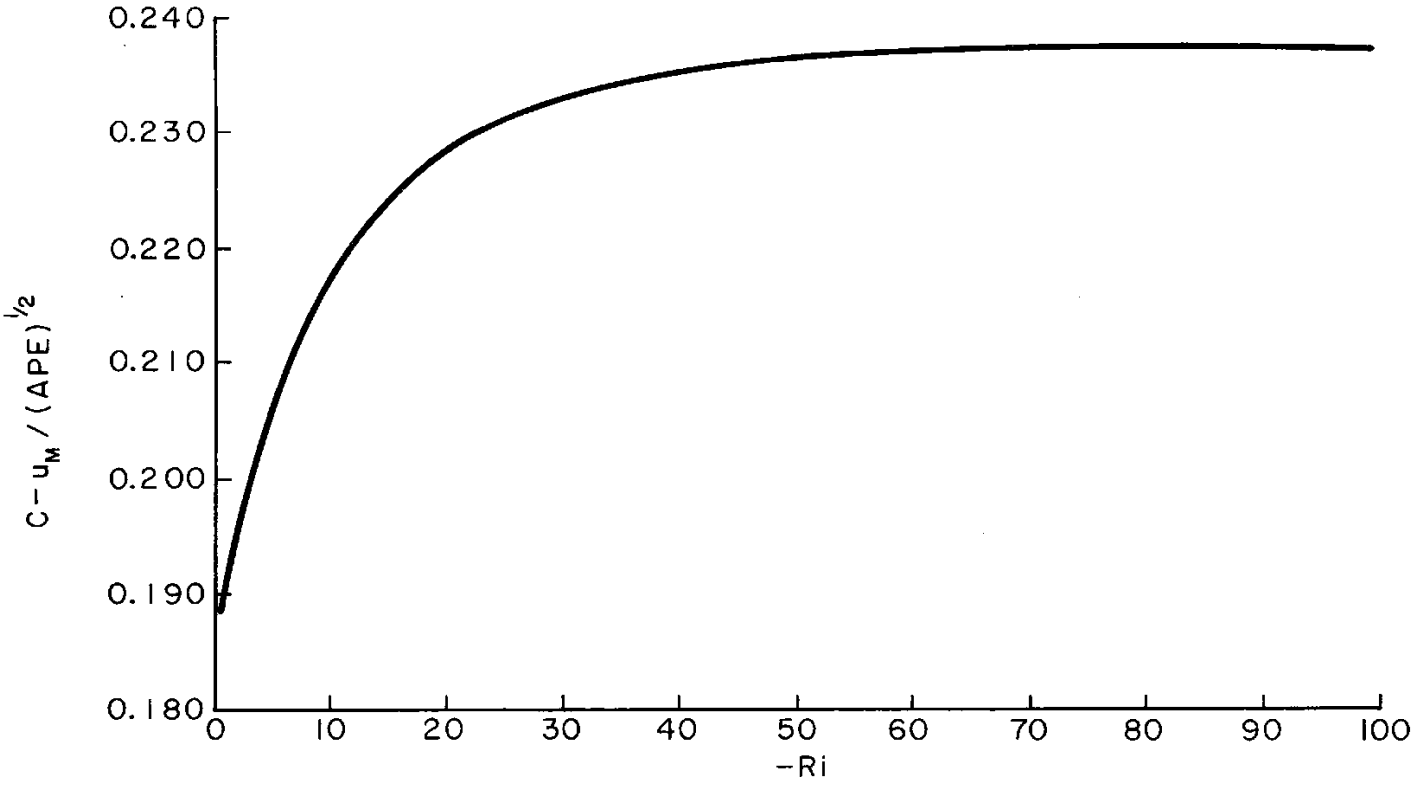

Figure 2.2 - Propagation speed vs.-Ri (after Moncrieff, 1974a).

As mentioned previously, the outflow velocity profile is also determined by the theory. The modification of the u component of the relative wind field by the cumulonimbus shown in Figure 2.1 is depicted in Figure 2.3. The outflow profiles for the observed storms (section 4.6) do not agree quantatively with theory. The difference in relative inflow velocity profiles (u component) between theory and observed (Figures 2.3 and 2.4) is responsible for the outflow profiles' incompatability. The theory has so far only been solved for simple symmetric wind profiles. This illustrates the need for further development of theory to find solutions for arbitrary inflow profiles.

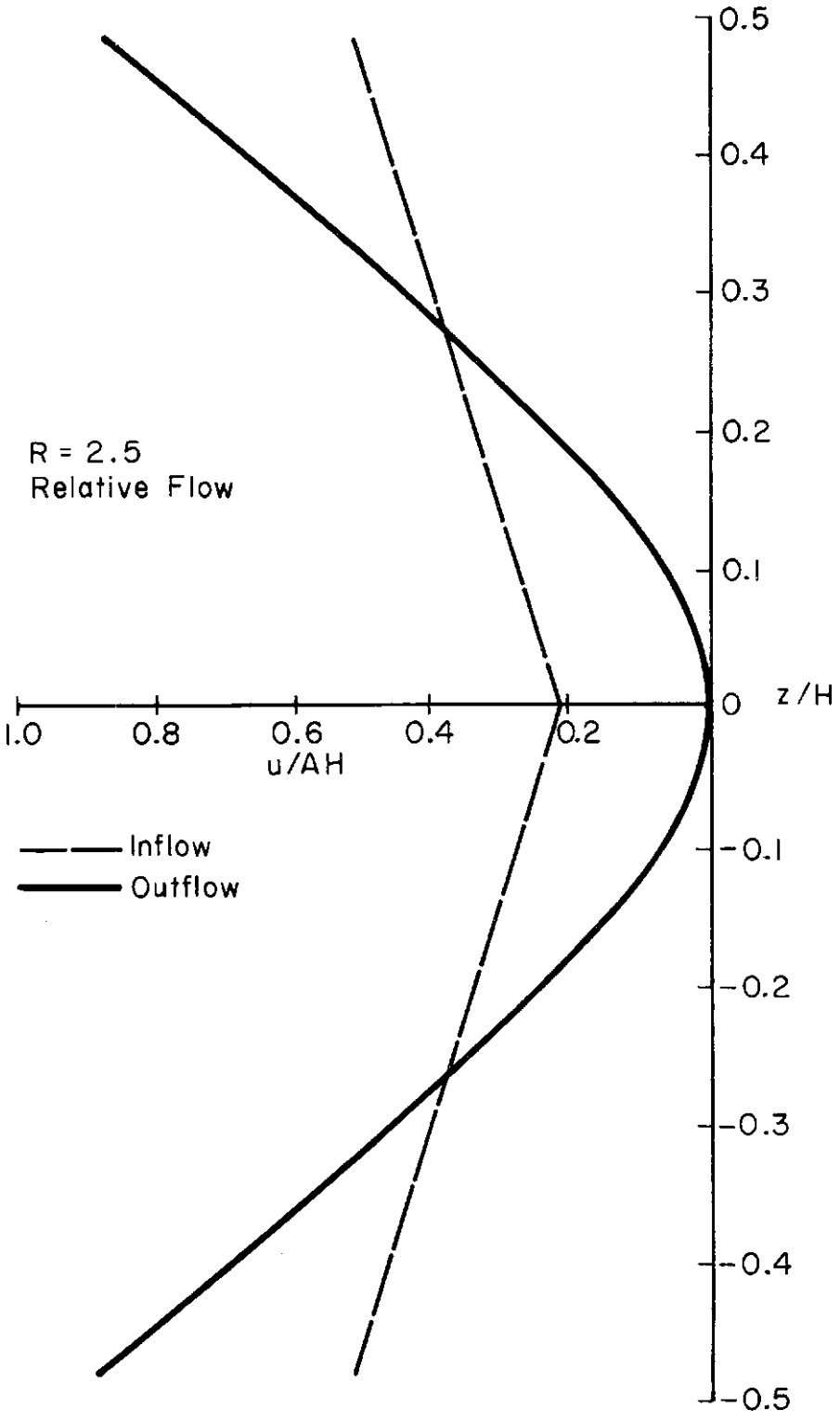

Figure 2.3 - Mean flow modification as predicted by the model (after Moncrieff, 1974a).

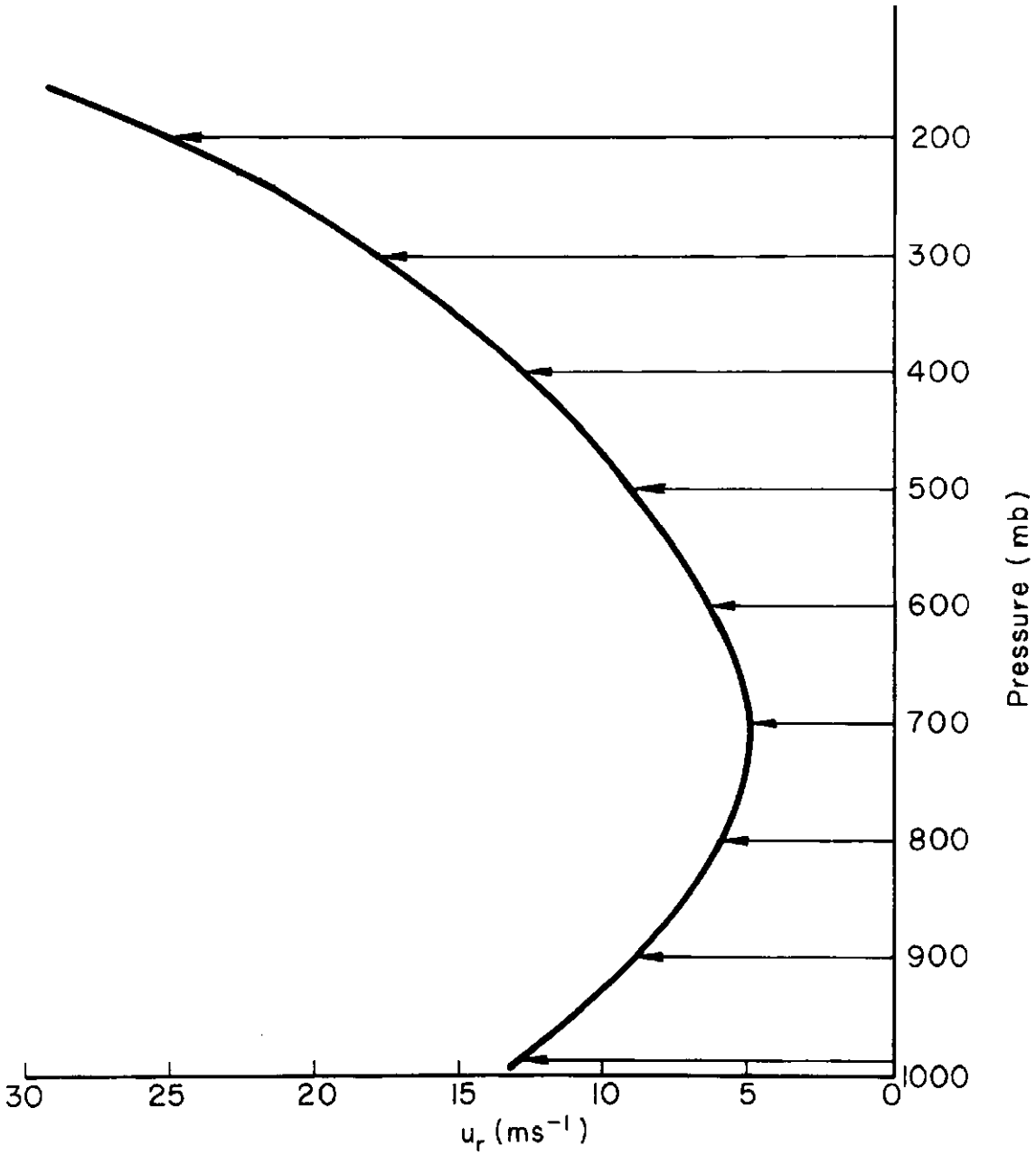

Figure 2.4. - Relative inflow velocity (u_r) profile of a squall-line.

3. PROCEDURE

3.1 General

As detailed in Chapter 2, the calculation of the Richardson Number involves numerous assumptions that may be applicable to the observed behavior of the storm systems. This chapter deals with the method used in computing the Richardson Number and its ramifications.

3.2 Richardson Number Computation

The Richardson Number as defined in section 2.2 is

$$\mathrm{Ri} = \int_{z_{0_*}}^{H} g(\phi_* - \phi)\,dz \quad \frac{1}{2}\left[\int_{z_{0_*}}^{H} \left(\frac{\partial u_{r0}}{\partial z}\right) dz\right]^2 \qquad 3.1$$

where the available potential energy is equal to the positive area of a thermodynamic diagram. Recalling that $\phi = \ln \theta$ then

$$d_\phi = d(\ln \theta) = d_\theta/\theta \qquad 3.2$$

thus,

$$\phi_* - \phi_0 = \frac{\Delta\theta}{\theta} \cong \frac{\Delta T}{T} \qquad 3\ 3$$

at constant pressure, where ΔT is the temperature difference between T of the parcel and T of the environment at a level. Thus, the available potential energy becomes

$$\mathrm{APE} = \int_{z_{0_*}}^{H} g\,\frac{\Delta T}{T}\,dz \qquad 3.4$$

Substituting the hydrostatic equation for dz in Eq. 3.4 and applying the equation of state

$$\mathrm{APE} = -\int_{z_{0*}}^{H} \left(\frac{R_d}{p}\right) \Delta T \, dp \qquad 3.5$$

where R_d is the gas constant for dry air. To compute the area delimited by the parcel/environmental curves on a thermodynamic diagram (Figure 3.1) an iterative scheme was used. Equation 3.5 is then

$$-\mathrm{APE} = \sum_{i=1}^{N} \left(\frac{R_d}{p}\right) \Delta T_i \left(p_{i+1} - p_{-1}\right) \qquad 3.6$$

where

$$\Delta \mathbf{T_i} = \mathbf{T}\,(\mathbf{P})_{\mathbf{M_i}} - \mathbf{T}\,(\mathbf{E})_{\mathbf{M_i}} =$$

$$\mathbf{.5}\left[\mathbf{T}\,(\mathbf{P})_{\mathbf{i+1}} + \mathbf{T}\,(\mathbf{P})_{\mathbf{i}} - \mathbf{T}\,(\mathbf{E})_{\mathbf{i+1}} - \mathbf{T}\,(\mathbf{E})_{\mathbf{i}}\right]$$

(see inset Figure 3.1). The summation is from i=1, cloud base (see section 3.4) to N, the equilibrium level of the parcel.

Moncrieff defines the available kinetic energy as

$$\mathrm{AKE} = \frac{1}{2}\left[\int_{z_{0*}}^{H} \left(\frac{\partial u_{r0}}{\partial z}\right) dz\right]^2 \qquad 3.7$$

For computational purposes, Moncrieff (1974b) defines Eq. 3.7 as

$$\mathbf{AKE} = \frac{\mathbf{1}}{\mathbf{2}}\left[\left(\overline{\frac{|\partial u_{r0}|}{\partial z}}\right)^{\mathbf{z_{0*}, H}}\right]^2 \Delta \mathbf{z_d}^2 \qquad 3.8$$

where $\Delta z = H - z_{0^*}$. With the conversion to pressure coordinates Eq. 3.8 becomes

$$\mathbf{AKE} = \frac{\mathbf{1}}{\mathbf{2}}\left[\left(\overline{\frac{|\partial u_{r0}|}{\partial p}}\right)^{\mathbf{p_{cb}, P_H}}\right]^2 \Delta \mathbf{p_d}^2 \qquad 3.9$$

where p_d equals the pressure at cloud base, p_{cb}, (see section 3.4) minus the equilibrium level of the parcel (p_H) and

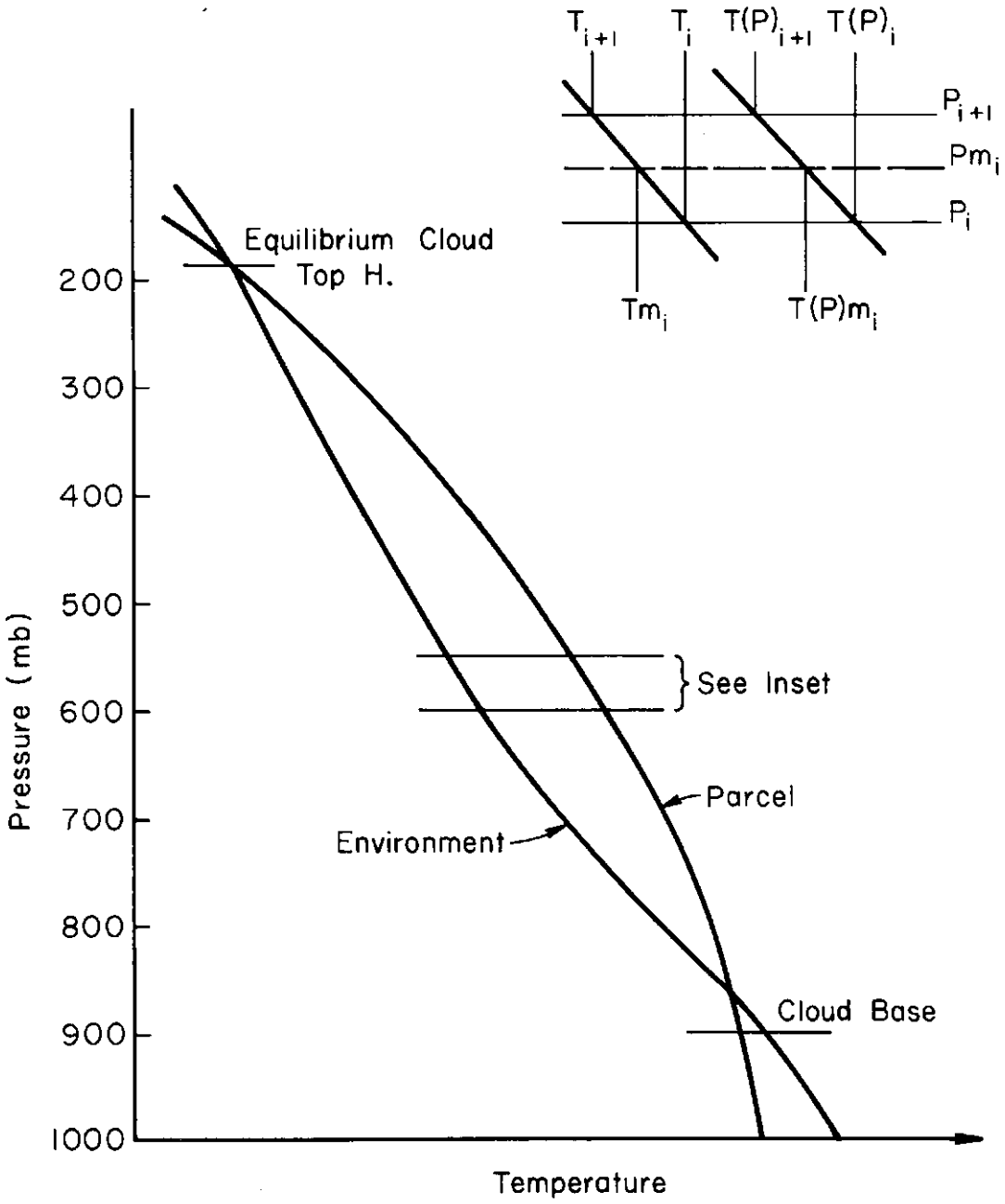

Figure 3.1 - Schematic diagram of parcel and environmental temperature profiles.

$$\left(\overline{\frac{|\partial u_{r0}|}{\partial p}}\right)^{p_{cb},P_H} = \left[\frac{\sum_{i=1}^{N} \frac{|u_{r0\,i+1} - u_{r0\,i}|}{p_{i+1} - p_i}}{N}\right] \qquad 3.10$$

Figure 3.2 is a schematic illustration of u_r. The inset shows how the summation was conducted.

The calculation of the Richardson Number reduces to division of the values obtained from Eq. 3.6 by those of Eq. 3.9.

3.3 Observed Storm Parameters

An observed parameter used by the model is the relative wind field of the storm. As stipulated by the model (Section 2.2) the coordinate axes were chosen to move with the propagation speed of the storm system such that relative to these axes the wind field is stationary.

Initial radiosonde measurements of the wind fields were relative to the earth. To obtain a u component wind field relative to the storm, the storm velocity was subtracted from the wind field and the resulting relative velocities were resolved along coordinates parallel and perpendicular to the storm motion. The relationship between a typical absolute u field (parallel to storm motion) and a u_r field for a cumulonimbus is shown in Figure 3.3. The vertical line at 13 ms^{-1} is the observed propagation speed of a cumulonimbus which was moving from east to west.

The observed propagation speed of a storm system is another parameter used in testing the model. To calculate the speed, the final radar position of the storm center was subtracted from the initial radar position. The resulting value was divided by the elapsed time between the two positions.

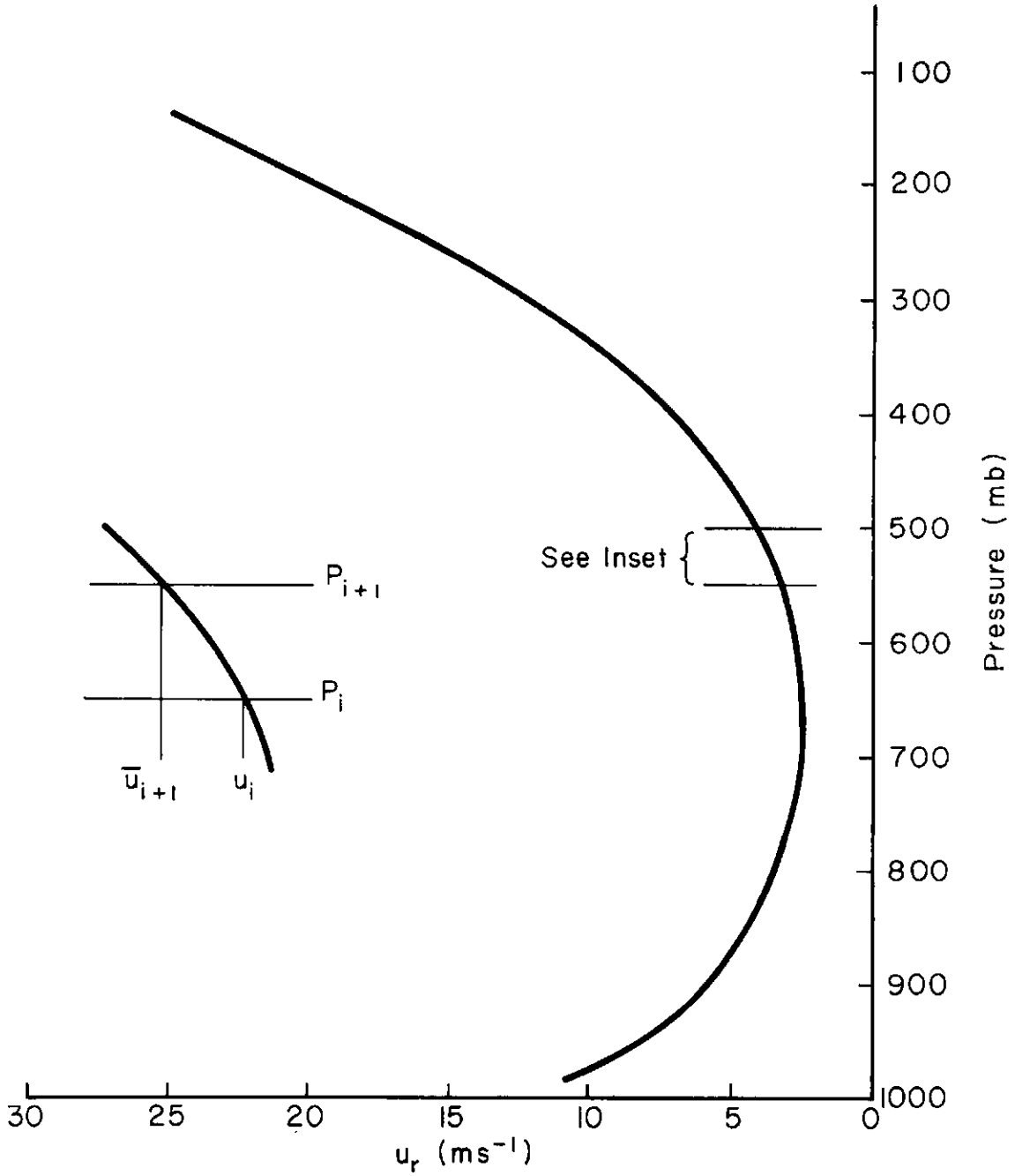

Figure 3.2 - Relative inflow velocity (u_r) profile.

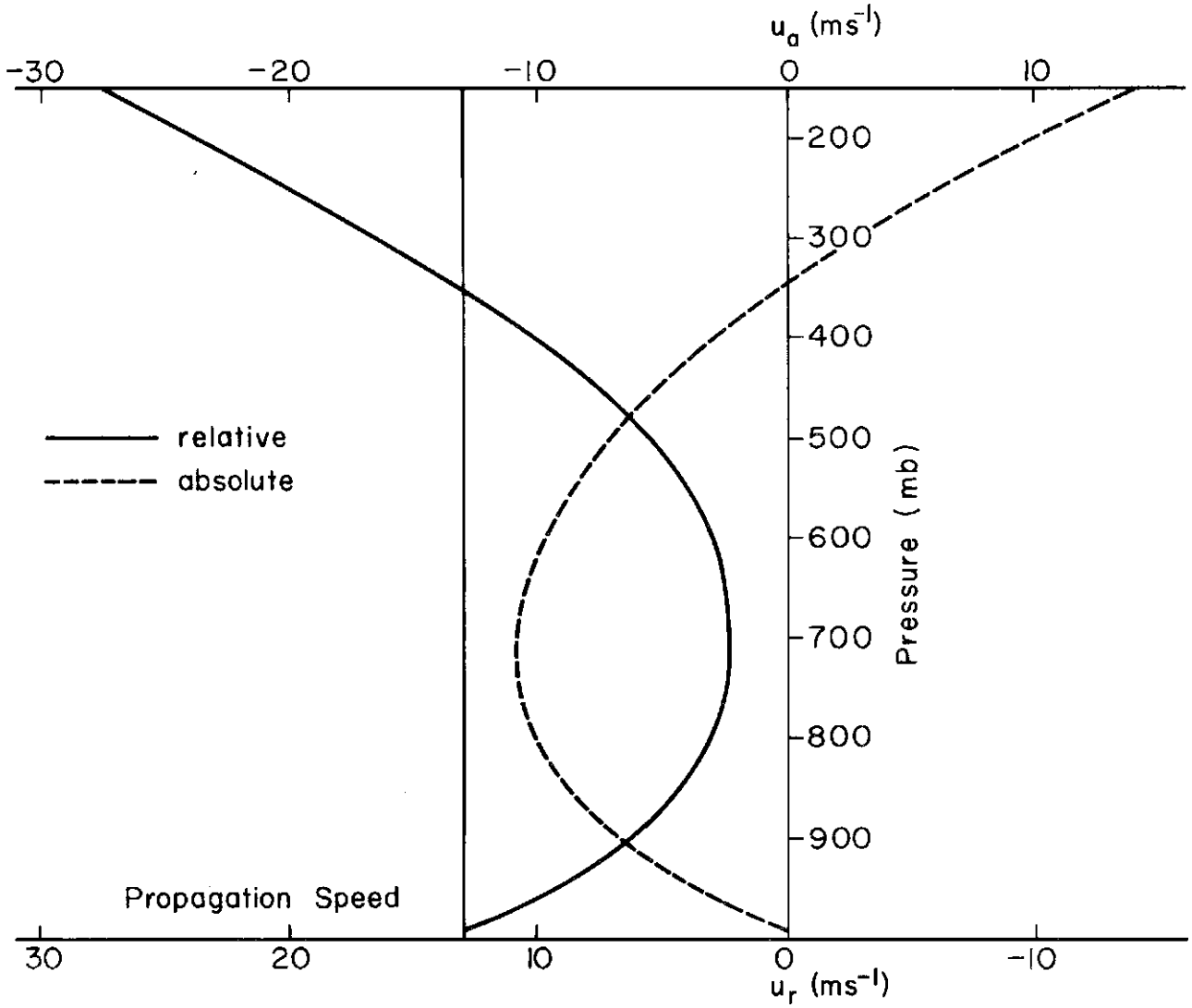

Figure 3.3 - Relationship between relative inflow (u_r) and absolute inflow (u_a). u_r is positive x-axis and $u_r = u_a - c$.

The accuracy of the propagation speed is determined by the accuracy with which the storm centers are measured. Plus or minus five kilometers results in an 8% error, or less than or equal to ±1 ms^{-1} error in the observed propagation speed.

The two final storm parameters are maximum area of the storm echo and the maximum cloud top, measured each fifteen minutes.

A potentially serious error of overestimation of the storm tops exists for the radar measured cloud tops. The detection by the side lobes of the 2° beam of higher reflectivity regions lower down in the storm when the beam axis is elevated above these regions can produce

exaggerations in the vertical height of the cloud (Atlas, 1972). From Figure 3.4, it is seen that beyond 57 km a 2° separation of beam axis and reflecting side lobe would generate a 2 km error in the cloud top. No means are available to determine the existence of this error in the measured cloud top used. However, it is thought that this error does not drastically affect the cloud top heights for reasons that become apparent in the following sections.

3.4 Available Potential and Kinetic Energy Variables

The only outflow level that can be consistently identified for the observed storms is that associated with maximum cloud top. By assuming the equilibrium level of the parcel corresponds to the maximum observed tops and these observed tops represent the outflow of the most buoyant air (assuming moist adiabatic ascent), then the inflow level of the highest θ_e air should replace z_Q in the calculation of the available potential energy. To select this high θ_e air, the θ_e values within the boundary layer having the lowest lifting condensation level (neglecting the surface value) were averaged. This average θ_e of the parcel ($\overline{\theta e}$) was

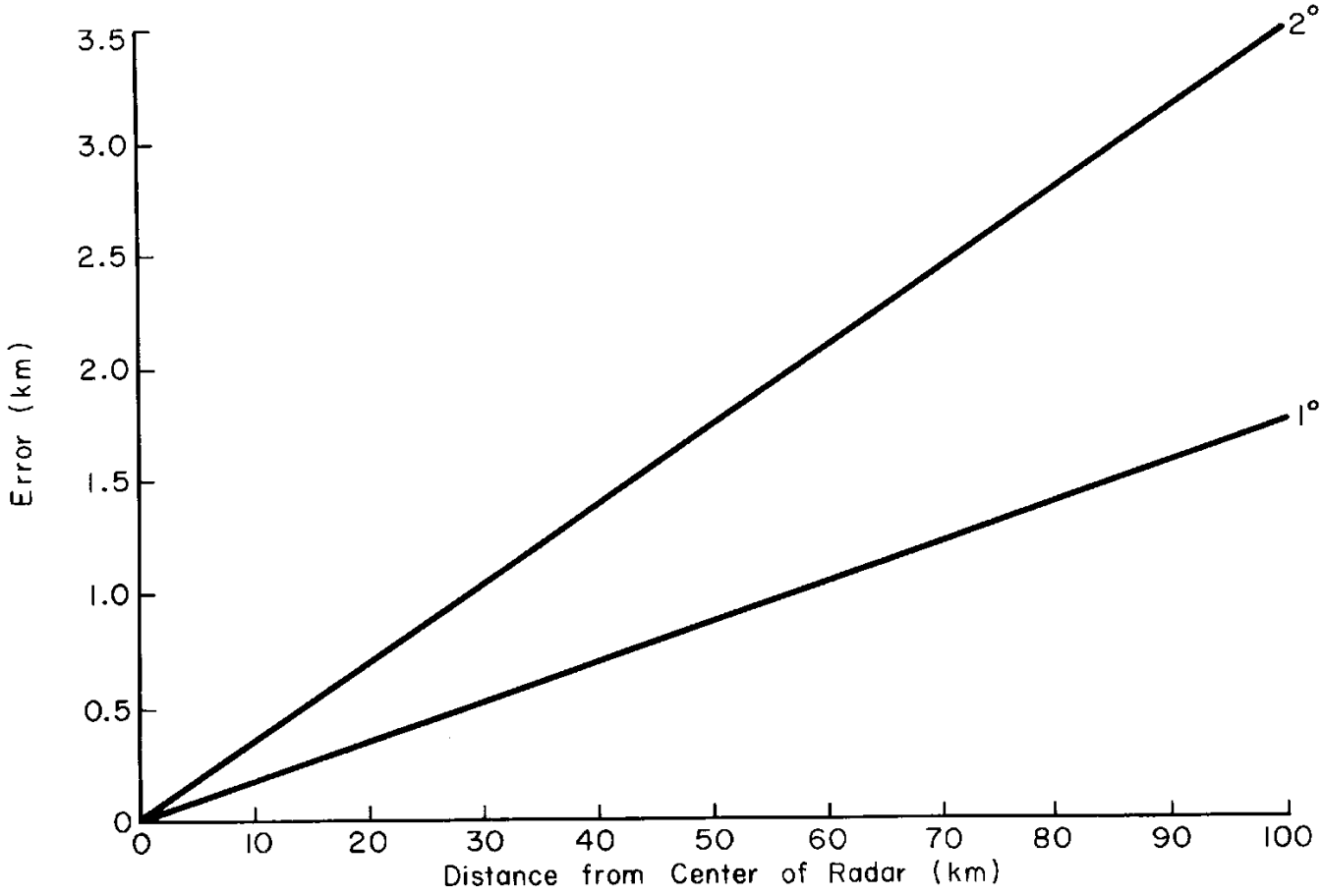

Figure 3.4 - Error in kilometers for 1° and 2° separation of beam axis and side lobe.

assumed saturated, i.e. $\overline{\theta e} = \theta_{es}$ (P), at 900 mb, a reasonable estimate of cloud base (Dugan, 1973); and was lifted along the saturated pseudo-adiabat until the equilibrium level of the parcel was reached.

Moncrieff, in his cumulonimbus model uses the limits z_{0^*} and H, where z_{0^*} is the mid-point of the boundary layer and H is the equilibrium level of the parcel, hereafter referred to as equilibrium cloud top. To compute a θ_e for z_{0^*}, Moncrieff averages θ_e from the surface to 900 mb and begins the parcel ascent at $z_{0^*} \simeq 950$ mb. Table 3.1 shows the parcel θ_e values computed from the inflow soundings of the fifteen storms. The first column ($\overline{\theta e}$) gives the parcel θ_e used in this study. The second column, θ_e (z_{0^*}), is the parcel θ_e computed using Moncrieff's method. With the exception of three cases, $\overline{\theta e} > \theta_e$ (z_{0^*}). Table 3.1 illustrates how the parcel θ_e can vary with different definitions.

For consistency, the available kinetic energy calculation used the same limits as were determined on a storm by storm basis for the available potential energy.

3.5 Adiabatic vs. Entrained Parcel Ascent

Thus far, adiabatic parcel ascent has been assumed. However, to test its validity, entrained equilibrium cloud tops were calculated using $\overline{\theta e}$ and compared against equilibrium cloud tops found by assuming adiabatic parcel ascent. Both cloud tops were in turn compared against the radar measured maximum cloud top for the entire storm and the average of the maximum cloud tops (15 minute values) during the mature stage of the storm's life cycle. Figure 3.5 shows the maximum cloud tops observed at 15 minute intervals for Storm 17. The growth, mature and decay phases of the system can be identified from this figure. The mature stage occurred between 1715 LST and 1812 LST. The heights during this interval

TABLE 3.1

Comparison of $\overline{\theta_e}$ With θ_e (z_{0^*})

Storm/Radiosonde	$\overline{\theta_e}$ °K	θ_e (z_{0^*}) °K
16/87	343.6	342.3
17/88	343.0	342.3
27/99	347.7	346.3
27/100	346.1	347.8
35/170	351.3	350.4
126/169	341.1	340.4
47/176	350.4	349.2
53/191	346.4	345.6
53/192	345.8	345.9
60/226	349.9	349.1
60/227	345.5	346.1
134/235	348.8	346.2
134/236	347.8	344.9
64/241	352.2	351.4
68/245	348.5	346.5
80/271	346.5	344.4
91/288	348.4	346.9
91/289	350.8	350.2
100/312	350.6	349.1
109/316	346.9	346.6

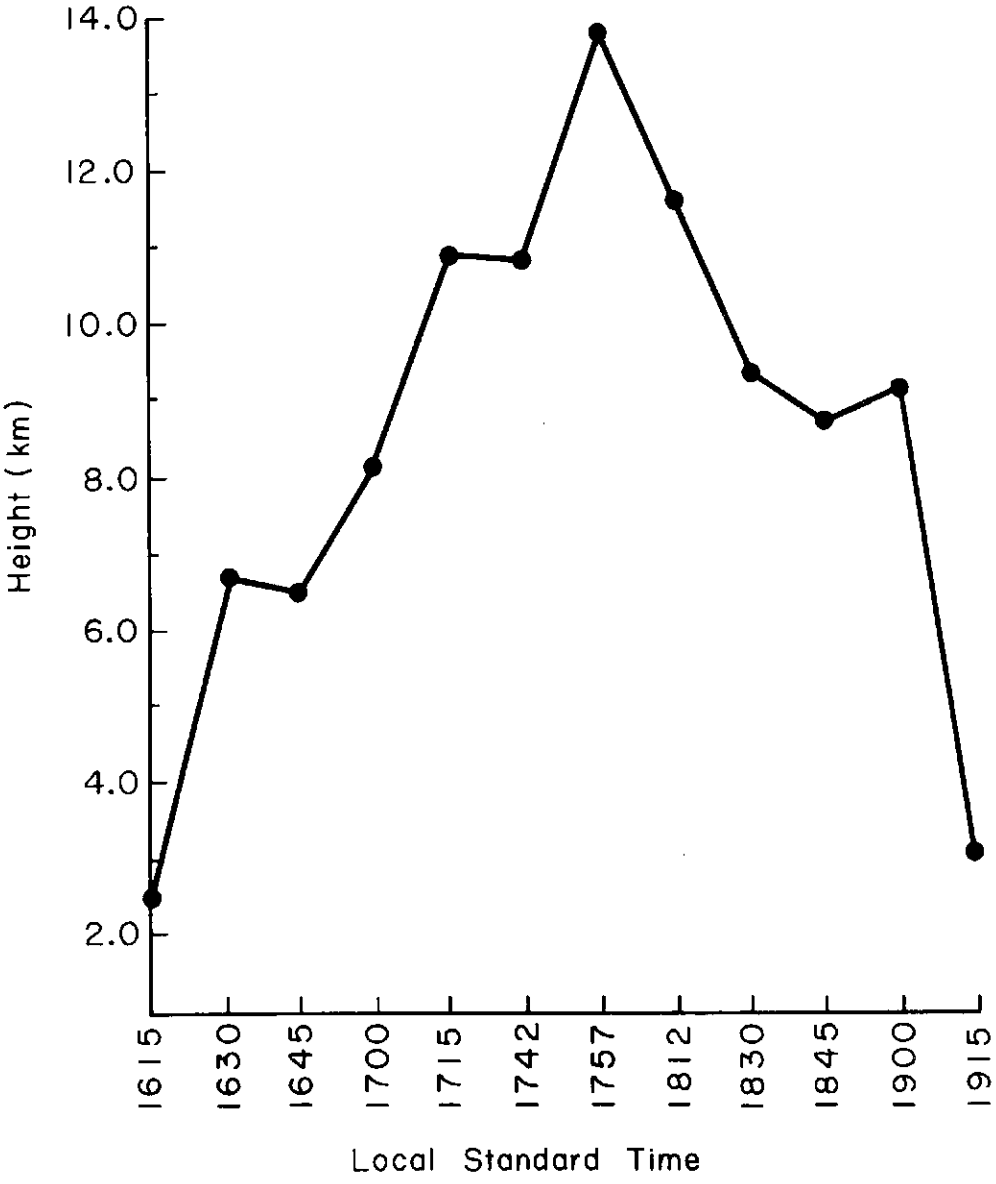

Figure 3.5 - Radar measured cloud top at 15 minute intervals for Storm 17.

were averaged to give the averaged maximum cloud top for this storm.

The entrained cloud tops were derived using.

$$\frac{d\theta_{es}(P)}{dp} = + \frac{1}{S_E}[\theta_e(E) - \theta_{es}(P)]$$

(Betts, 1973a) where $S_E = (\Delta p)(x)$. Δp is the depth of the storm system (cloud base to cloud top) and x is the entrainment factor, x was varied for 1.0 to 4.0 at 0.5 intervals: x = 1.0 implies greater entrainment, hence a lower cloud top than x = 4.0.

To determine which predicted set of cloud tops correlated best with which set of measured cloud tops, Mielke (1974) suggested that the means of the sum of the absolute value of the difference between measured cloud top and predicted cloud top be compared. The smallest mean would represent the best correlation. Table 3.2 shows the means calculated. The adiabatically determined cloud top and averaged maximum cloud top

correlate best.

TABLE 3.2

Correlation Results for Predicted and Measured Cloud Top

	Entrainment Factor x							Adiabatic
	1.0	1.5	2.0	2.5	3.0	3.5	4.0	∞
Maximum Cloud Top	380.75	235.75	172.00	157.00	150.75	134.75	129.75	80.65
Averaged Maximum Cloud Top	335.50	205.75	140.00	132.50	129.00	113.75	107.25	67.15

Table 3.3 shows the adiabatic equilibrium cloud tops for each storm system. Figure 3.6 shows the frequency distribution of the Δp in Table 3.3.

The correlation of these particular values shows that probably 1) saturated pseudo-adiabatic ascent of the parcel is a valid assumption for the tropical storm systems under study and 2) the overestimation error of radar top discussed previously is not a serious problem with these fifteen storms. However, only the observed tops were available and these may be somewhat higher than the main outflow level.

3.6 Errors in APE, AKE and Ri

The largest error in the Richardson Number is found in the selection of $\overline{\theta_e}$ for available potential energy. $\overline{\theta_e}$ may be in error by as much as ± 0.5 K. A 0.5 K change of $\overline{\theta_e}$ may change the available potential energy by as much as 20%, depending upon the particular storm. This illustrates the sensitivity of the available potential energy to $\overline{\theta_e}$. As a result, every effort was made to ensure the use of error-free $\overline{\theta_e}$ values.

There are two potential errors in available kinetic energy. The first is due to the ± 0.5 K $\overline{\theta_e}$ error in the available kinetic energy. Depending upon the u_r wind profile for a storm, a change in H due to a ± 0.5 K $\overline{\theta_e}$ error could change the available kinetic energy a few percent, up to >50%. The second error is due to an ~± 1 ms^{-1} error in the measurement of the winds. The analytical analysis of this error is more difficult. However, this error probably did not exceed 20%.

The Richardson Number will reflect the errors in the available potential and kinetic energies. The value of the Richardson Number calculated would generally not be in error by >20%.

TABLE 3.3

Predicted and Measured Cloud Top

Storm/Radiosonde	Averaged Maximum Cloud Top Pressure Level (mb)	Adiabatic Cloud Top Pressure Level (mb)	Δp* (mb)
16/87	200	375	-175
17/88	200	375	-175
27/99	245	215	+30
27/100	245	250	- 5
35/120	150	170	- 20
126/169	265	395	-130
47/176	310	185	+125
53/191	145	250	-105
53/192	145	300	-155
60/226	355	175	+180
60/227	355	190	+165
134/235	195	160	+ 35
134/236	195	180	+ 15
64/241	135	130	+ 5
68/245	130	165	- 35
80/271	215	205	+ 10
91/288	125	150	- 25
91/289	125	136	- 11
108/312	135	142	- 7
109/316	195	160	+ 35

*Δp= average maximum cloud top - adiabatic cloud top

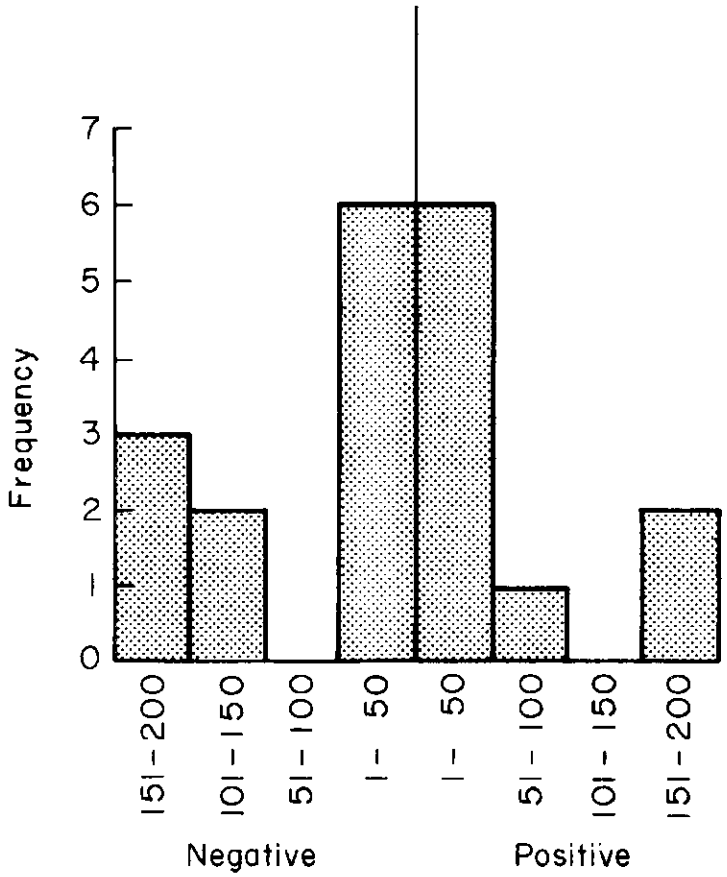

Figure 3.6 - Frequency distribution of Δp.

4. RESULTS

4.1 General

Summarized in Section 1.3, Table 1.2, are the specific characteristics used to distinguish the three classes of storm systems. The squall-lines (Group 1) were found to have a Richardson Number £-0.93, inflow into the front of the system at all levels, a trough at 850 mb that was associated with their occurrence, a definite line configuration, observed propagation speeds that correlated with the predicted propagation speeds and an atmosphere that was strongly modified as a result of their passage. The non-squall-lines (Group 2) and the large non-propagating mesosystems (Group 3) did not in general have these characteristics.

This chapter will discuss the characteristic features mentioned above that led to the classification of the fifteen storm systems. Furthermore, based upon a composite of the inflow and outflow atmosphere soundings of the squall-lines a observational model of a squall-line is presented.

4.2 Richardson Number

The results of computing the Richardson Number (as outlined in Section 3.2) for each of the fifteen storms are presented in Table 4.1. These results have been ordered by the magnitude of the Richardson Number. As discussed in Section 3.6, these values of Ri are typically good to about 20%. These values alone, do not uniquely identify the different groups.

TABLE 4.1

Richardson Numbers for Storm Set

Richardson Number	Storm Number/ Radiosonde Number
-0.26	17/88
-0.37	126/169
-0.62	16/87
-0.67	80/271
-0.69	134/235
-0.70	53/191
-0.91	68/245
-0.93	27/99 *
-0.95	60/226*
-1.1	47/176*
-1.1	27/100*
-1.3	134/236
-1.5	60/227*
-1.7	109/316
-2.0	35/120*
-2.1	91/289*
-2.3	91/288*
-3.0	53/192
-3.1	64/241*
-3.5	108/312

*Group 1 storms (true squall-lines).

In eight storms, the adiabatically derived cloud tops differ significantly (> ±100 mb) from the averaged maximum cloud top (Table 3.3), suggesting the inflow $\overline{\theta e}$ value chosen is not representative of the inflow air. This would affect the Richardson Number of these eight storms. To calculate Ri corresponding to the averaged maximum cloud tops, $\theta_{es}(E)_{CT} = \theta_{es}(P)_{CT}$ (CT =cloud top) was assumed at cloud top. This $\theta_{es}(P)_{CT}$ replaced $\theta_{es}(P)$, derived from $\overline{\theta e}$, at 900 mb in the available potential energy calculation (Section 3.2). The available potential and kinetic energies were summed from 900 mb to the averaged maximum cloud top. The new Richardson Number for the eight storms derived from observed cloud top are presented in Table 4.2.

TABLE 4.2

Ri For Averaged Maximum Cloud Top

Storm Number/ Radiosonde Number	Δp (mb)	Ri From Observed Inflow Data	Ri From Observed Top Heights
17/88	-175	-0.26	-0.59
126/169	-130	-0.37	-0.58
16/87	-175	-0.62	-0.79
53/191	-105	-0.70	-1.3
53/192	-155	-3.0	-0.76
47/176	+125	-1.1	+0.29
60/226	+180	-0.95	-0.35
60/227	+160	-1.5	-0.66

The negative Δp values, with the exception of that for 53/192, show an increased Ri. Storm 53/192, because of its unusual u_r profile and temperature lapse rate, showed a decreased Ri.

The reason for Storm 47 and 60's decreased Ri for a positive Δp can be found in the upper level wind fields rather than in their $\overline{\theta e}$ value. The strong upper level flow on the order of 30 ms^{-1} at 150 mb for 47

and 42 ms^{-1} at 150 mb for 60 suggests that shearing by the westerlies can, in certain instances, limit the depth of convective penetration. Subsequently, the Richardson Number obtained using adiabatic cloud top will be retained for storms 47 and 60.

Presented in Table 4.3 is the best estimate of the Richardson Number for the fifteen storms. While no absolute group classification can be applied to the Richardson Numbers in this table, all six squall-lines (Group 1) do have $Ri \leq -0.93$, and seven out of nine of the non-squall-line storm systems (Group 2) have $Ri \geq -0.91$. Considering the potential errors associated with the calculations, this separation seems quite significant.

4.3 Synoptic Evaluation

From examination of the synoptic charts (analyzed by Dr. H. Riehl) for each of the three groups, synoptic conditions characteristic of each group could be identified. Space limitations prevent the presentation of every storm's synoptic pattern; therefore, an example that typifies each group is presented.

Storm 47 is representative of Group 1. It appears on the radar at 1615 LST on the 24th of July. For a discussion of its geometric characteristics, see Section 4.4.

Figures 4.1, 4.2 and 4.3 show the isobaric pattern for Storm 47 at 1200 Z (0800 LST) on July 24th for 200 mb, 500 mb and 850 mb respectively. The 200 mb pattern shows a trough has moved through north-central Venezuela in the past twelve hours and is traveling east into the Atlantic. The 500 mb chart shows a high pressure dominating the entire Caribbean and the north-central South American continent. The 850 mb

TABLE 4.3

Best Estimate of Ri for Storm Set

Richardson Number	Storm Number/ Radiosonde Number
-0.58	126/169
-0.59	17/88
-0.67	80/271
-0.69	134/235
-0.76	53/192
-0.79	16/87
-0.91	68/245
-0.93	27/99 *
-0.95	60/226*
-1.1	47/176*
-1.1	27/100*
-1.3	134/236
-1.3	53/191
-1.5	60/227*
-1.7	109/316
-2.0	35/120*
-2.1	91/289*
-2.3	91/288*
-3.1	64/241*
-3.5	108/312

*Group 1 (true squall-1ines).

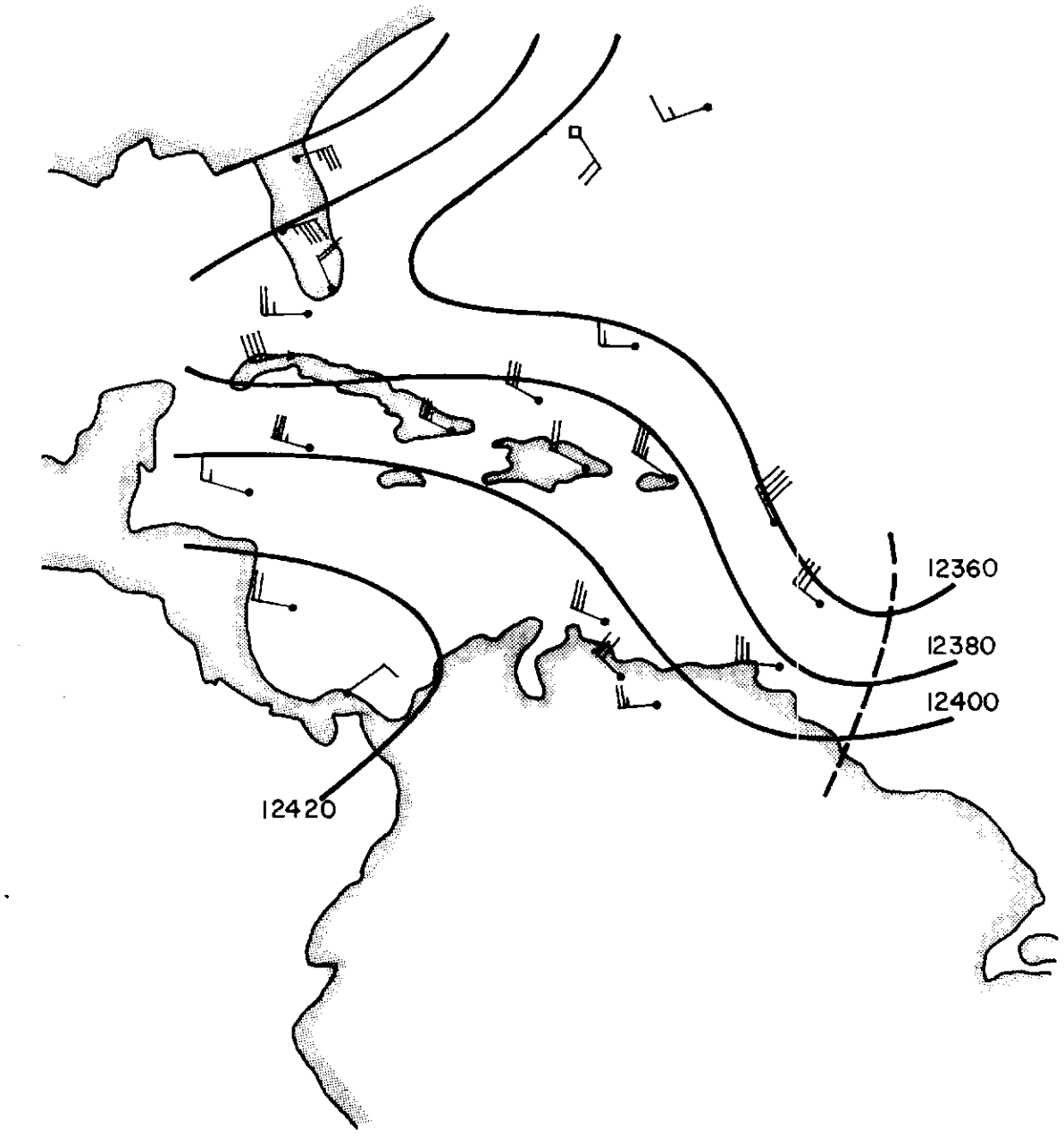

Figure 4.1 - Height pattern on 200 mb surface at 1200 Z,
July 24, 1972.

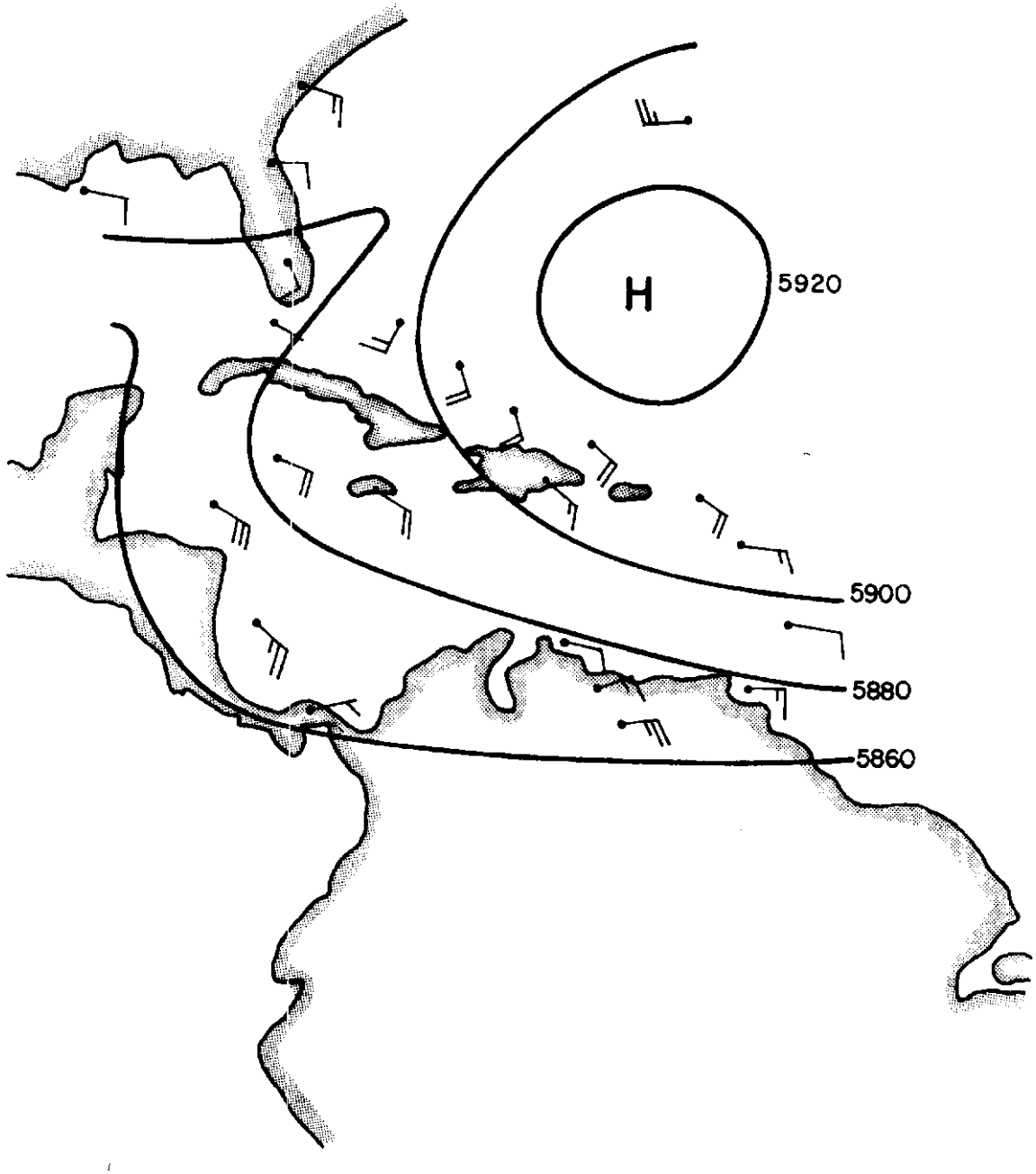

Figure 4.2 - Height pattern on 500 mb surface at 1200 Z,
July 24, 1972.

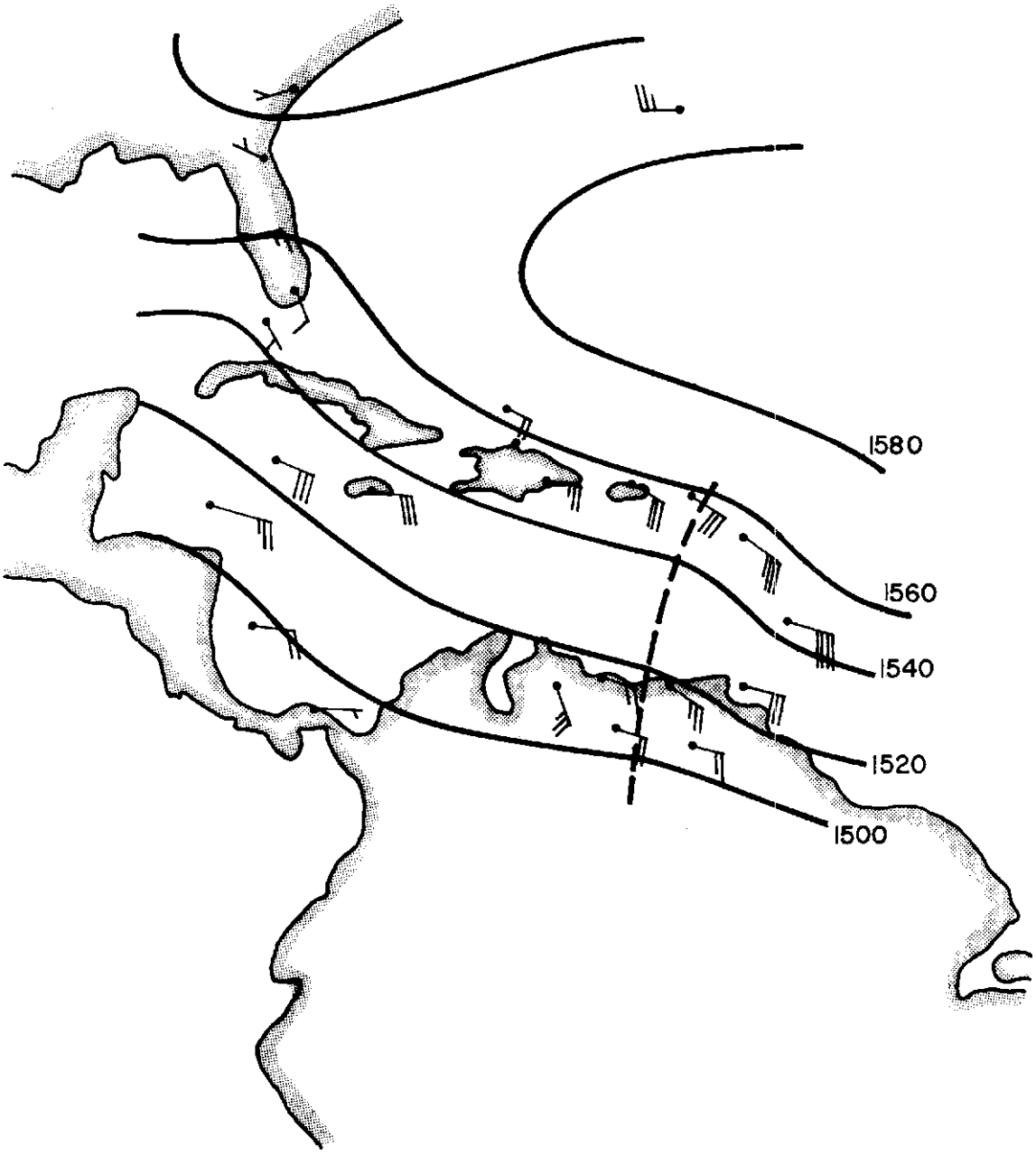

Figure 4.3 - Height pattern on 850 mb surface at 1200 Z,
July 24, 1972.

chart contains the most significant feature observed with the occurrence of these six storm systems. This is the passage of the 850 mb trough through the north-central section of South America. The 850 mb charts for three of the remaining five Group 1 squall-lines showed such a trough. For the remaining two storms (27 and 64) no trough could be identified from the synoptic data available. This trough is probably responsible for the triggering of the squall-line by supplying the necessary low level convergence.

The synoptic pattern for Group 2 storms differed from that for Group 1. A typical example is Storm 68 (discussed in Section 4.4). Figures 4.4, 4.5 and 4.6 show the synoptic situation at 1200 Z on the 12th of August at 200 mb, 500 mb, and 850 mb levels.

The 200 mb level shows there is a high pressure dome over Venezuela at 1200 Z, while at 500 mb a ridge is approaching the South American continent from the Atlantic. The 850 mb chart shows a ridge moving with the 500 mb ridge toward South America.

The synoptic situation illustrated in Figures 4.4 through 4.6 existed to varying degrees for all of Group 2 storms. Missing in Group 2 storms was the 850 mb trough associated with Group 1 storms. Storms 108 and 109 warrant comment because of their unique character. These two storms were the largest observed during the summer. Storm 109 at its peak (0730 LST) had an area of at least 11,655 km^2, with additional area beyond radar range. This is in sharp contrast to Storm 47, the maximum area of which was only 2554 km^2. Storm 108 began at 2115 LST on September 1st and continued until 0300 LST on the 2nd. Forty-five minutes later, Storm 109 began and lasted until 1415 LST the same day. Figure 4.7 shows Storm 109 at 0800 LST close to the 1200 Z

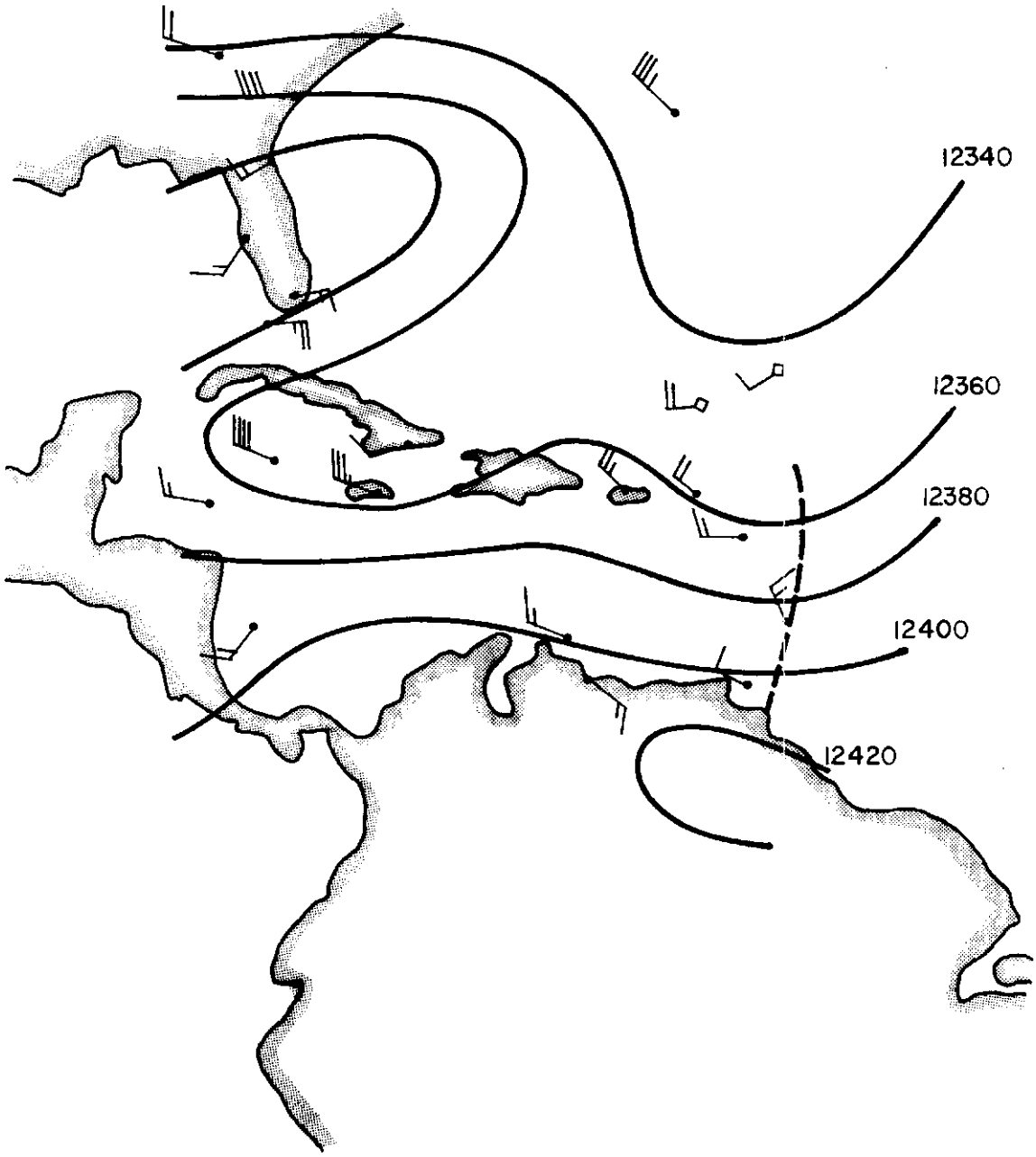

Figure 4.4 - Height pattern on 200 mb surface at 1200 Z, August 12, 1972.

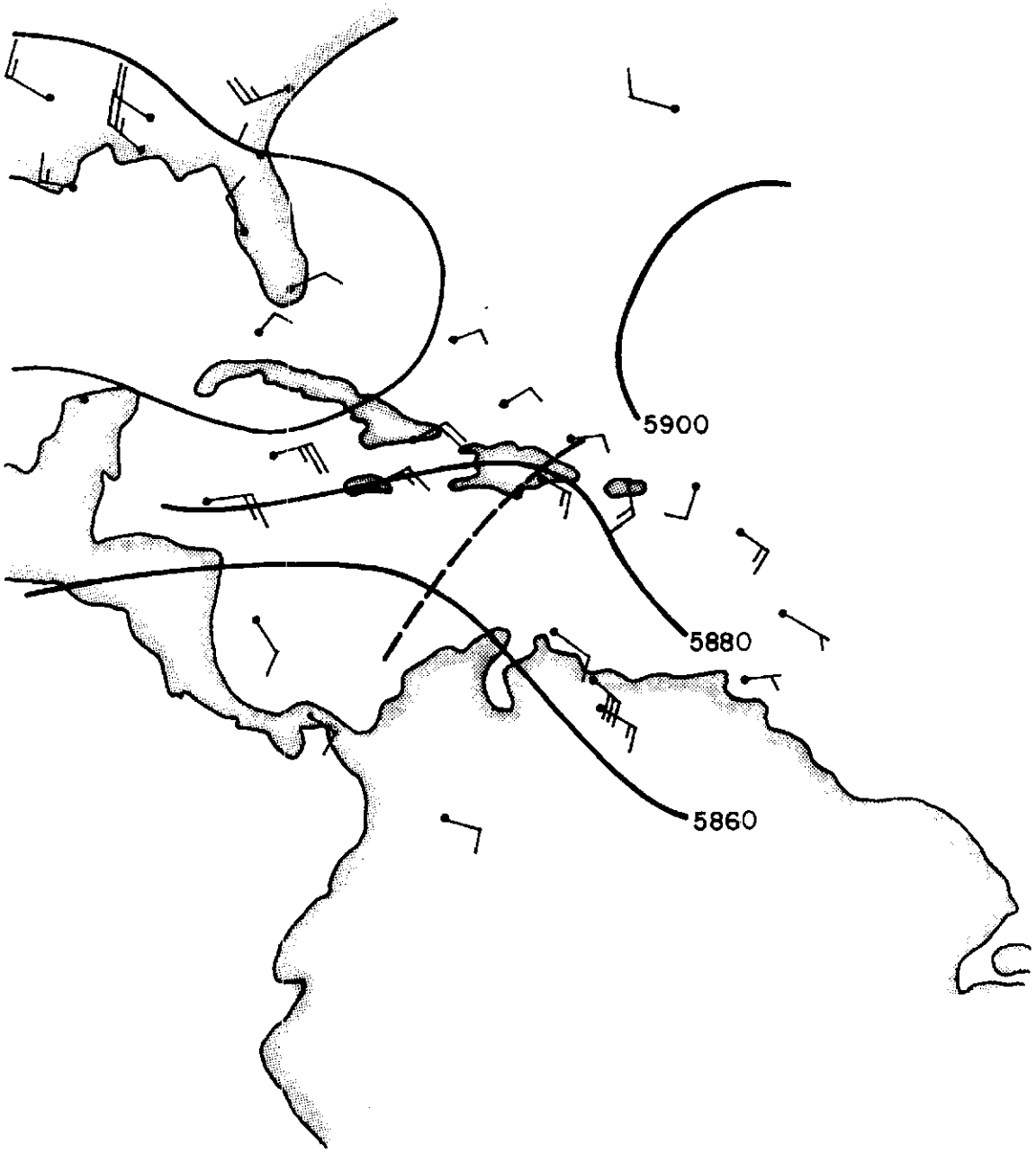

Figure 4.5 - Height pattern on 500 mb surface at 1200 Z,
August 12, 1972.

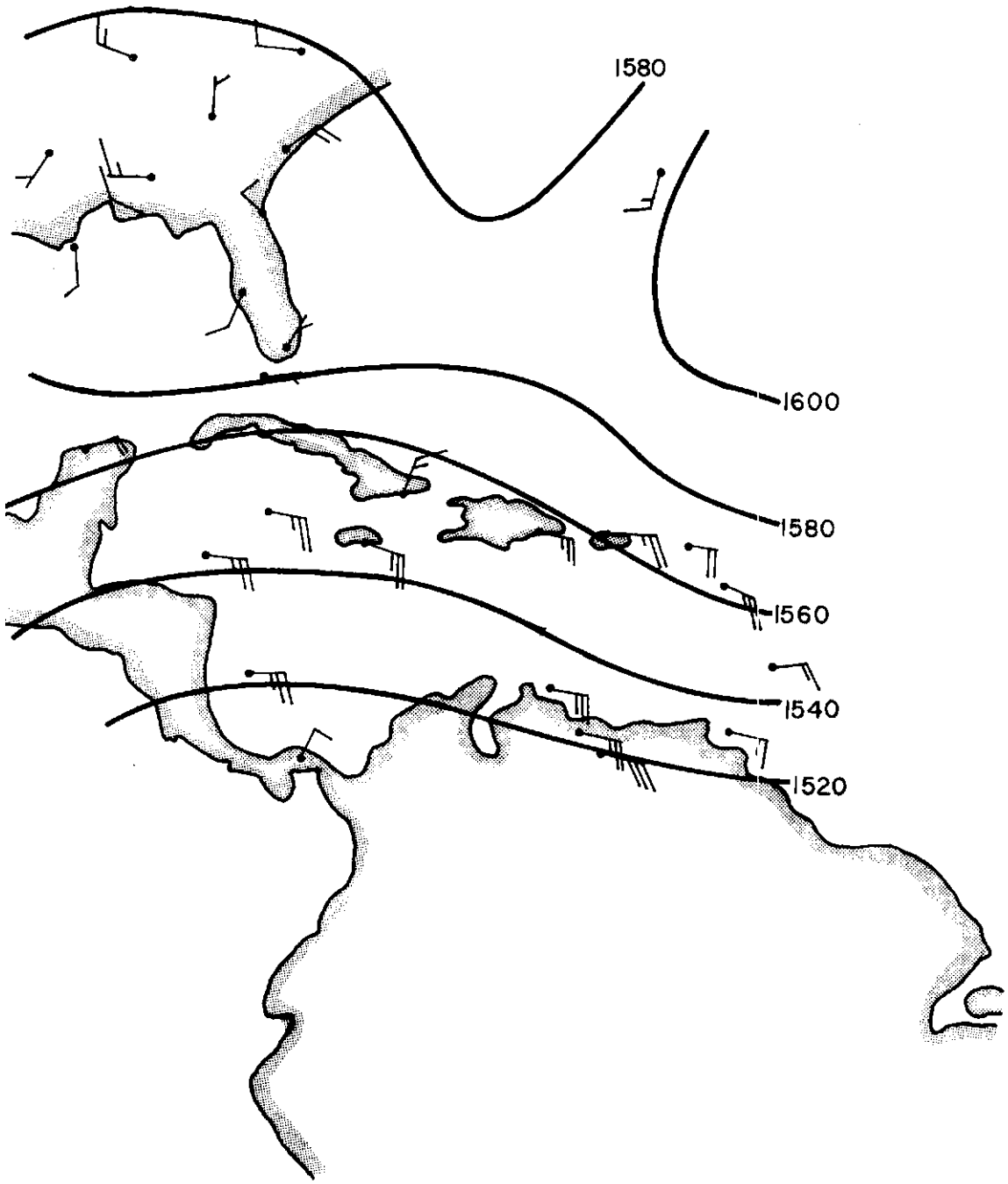

Figure 4.6 - Height pattern on 850 mb surface at 1200 Z, August 12, 1972.

synoptic time. Because of its size and duration, the storm is not presented in its entirety. It is of interest to note that both the beginning and end of 108 and 109 were recorded on film and at no time did the systems travel beyond radar range.

Shown in Figures 4.8, 4.9 and 4.10 is the synoptic situation at 1200 Z on September 2nd. At 200 mb a trough can be seen extending from mid-Atlantic southwest over Venezuela. The 500 mb chart shows a most interesting pattern. Two troughs are associated with a low pressure centered over the radar site. At 850 mb a trough associated with a low pressure over the Panama Canal has just passed over the radar site. This low pressure can be seen at 500 mb. Presumably, the duration, intensity, size and lack of propagation of these two storms can be attributed to the unusual synoptic situation.

4.4 Geometric and Dynamic Characteristics

Storms 47 and 68 will again be used to illustrate the geometric and dynamic characteristics of Group 1 and Group 2. Figure 4.11 shows the radar composite for Storm 47 at half-hour intervals from when it first appeared on the radar at 1615 LST. There is a defined squall front to this storm, which was characteristics of all Group 1 storms. To be considered a quasi-steady state system, the storm should show little change of shape during the sampling of its inflow environment. Figure 4.11 shows little change in Storm 47 for the two echos photographed immediately prior to the storm passing the radar site. This quasi-steady feature, particularly during the inflow sampling, was exhibited by each Group 1 storm. The final important characteristic of Group 1 storms was the line configuration along their major axes, which

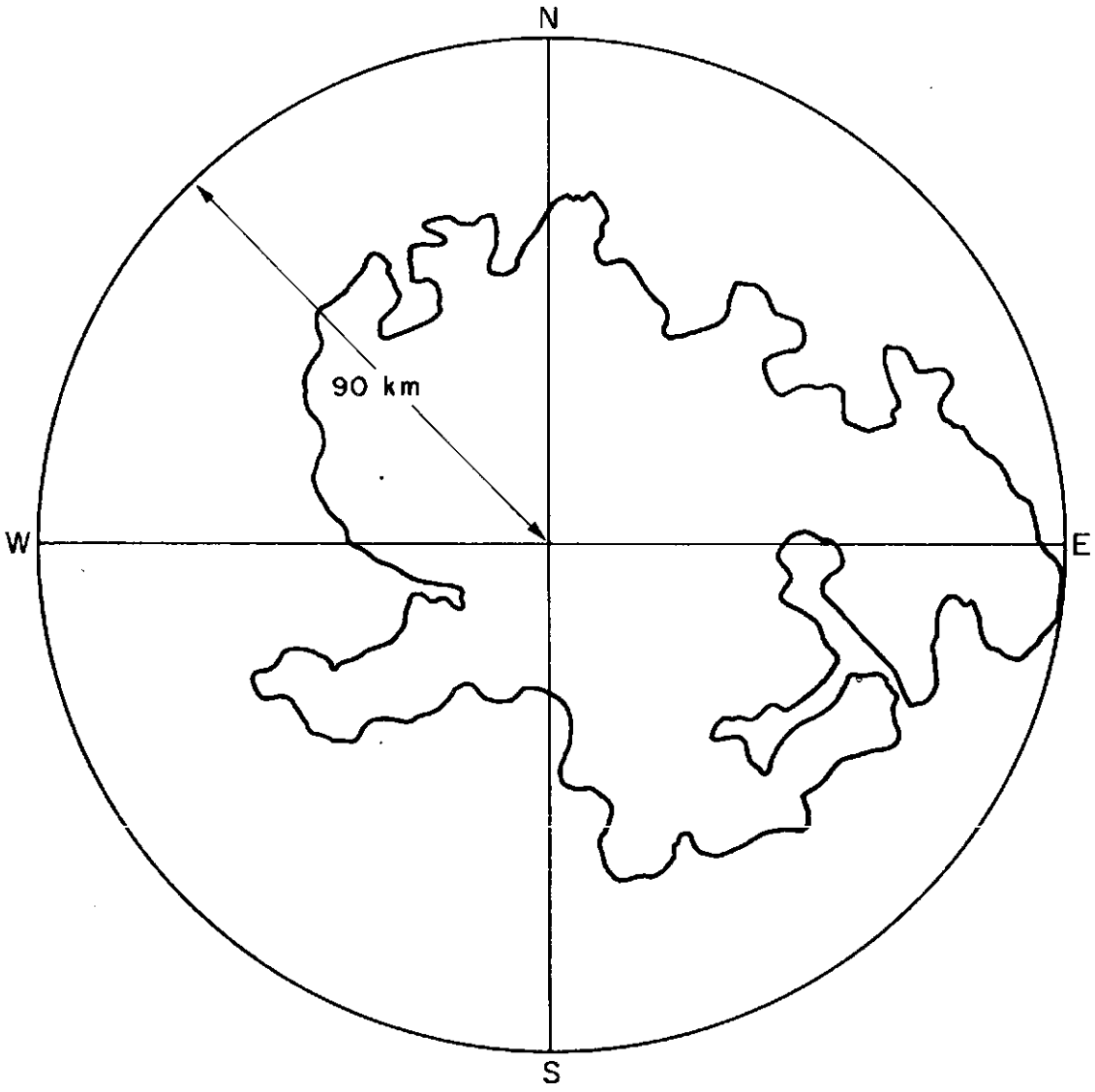

Figure 4.7 - Storm 109 at 0800 LST on September 2nd.

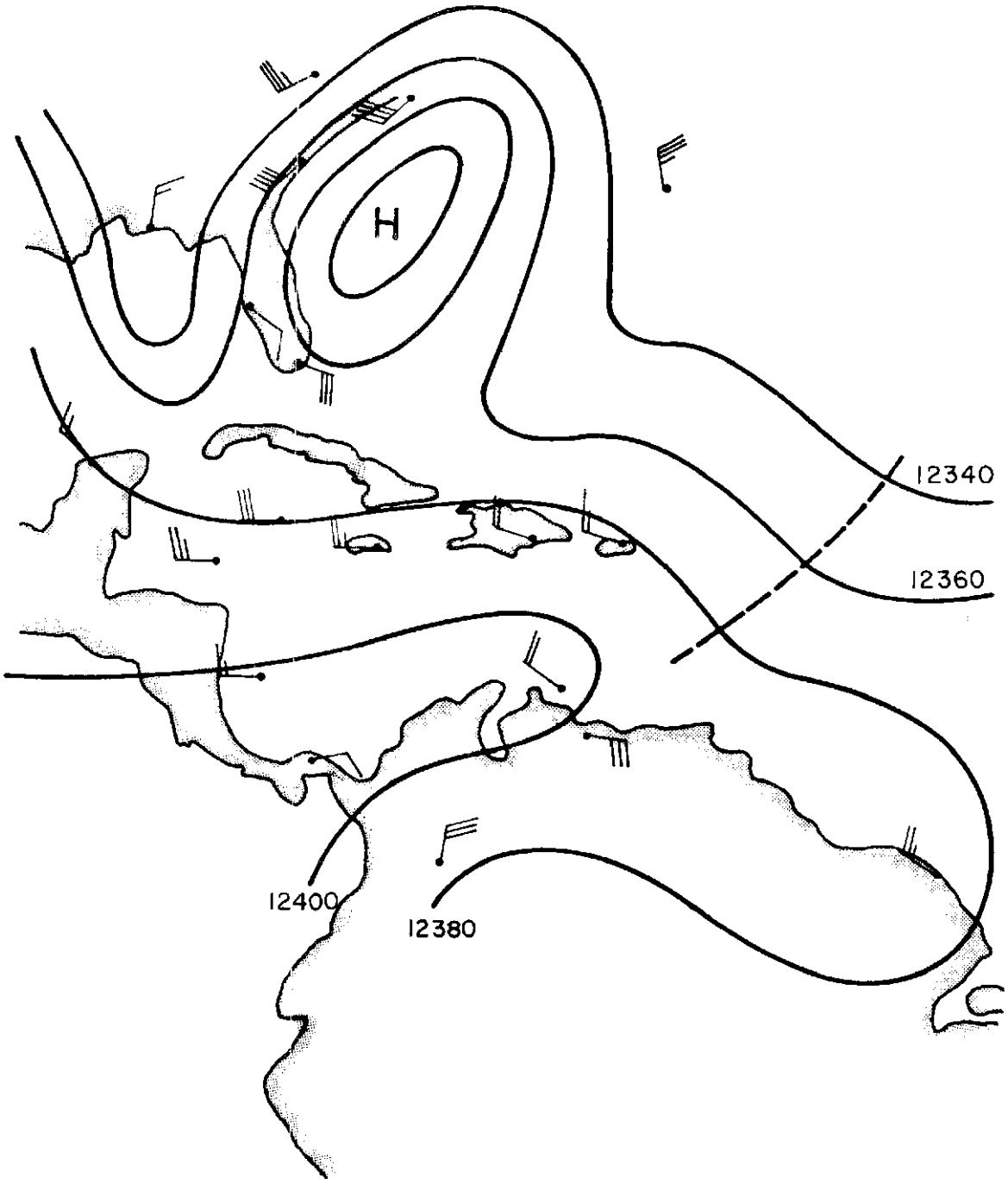

Figure 4.8 - Height pattern on 200 mb surface at 1200 Z,
September, 2, 1972.

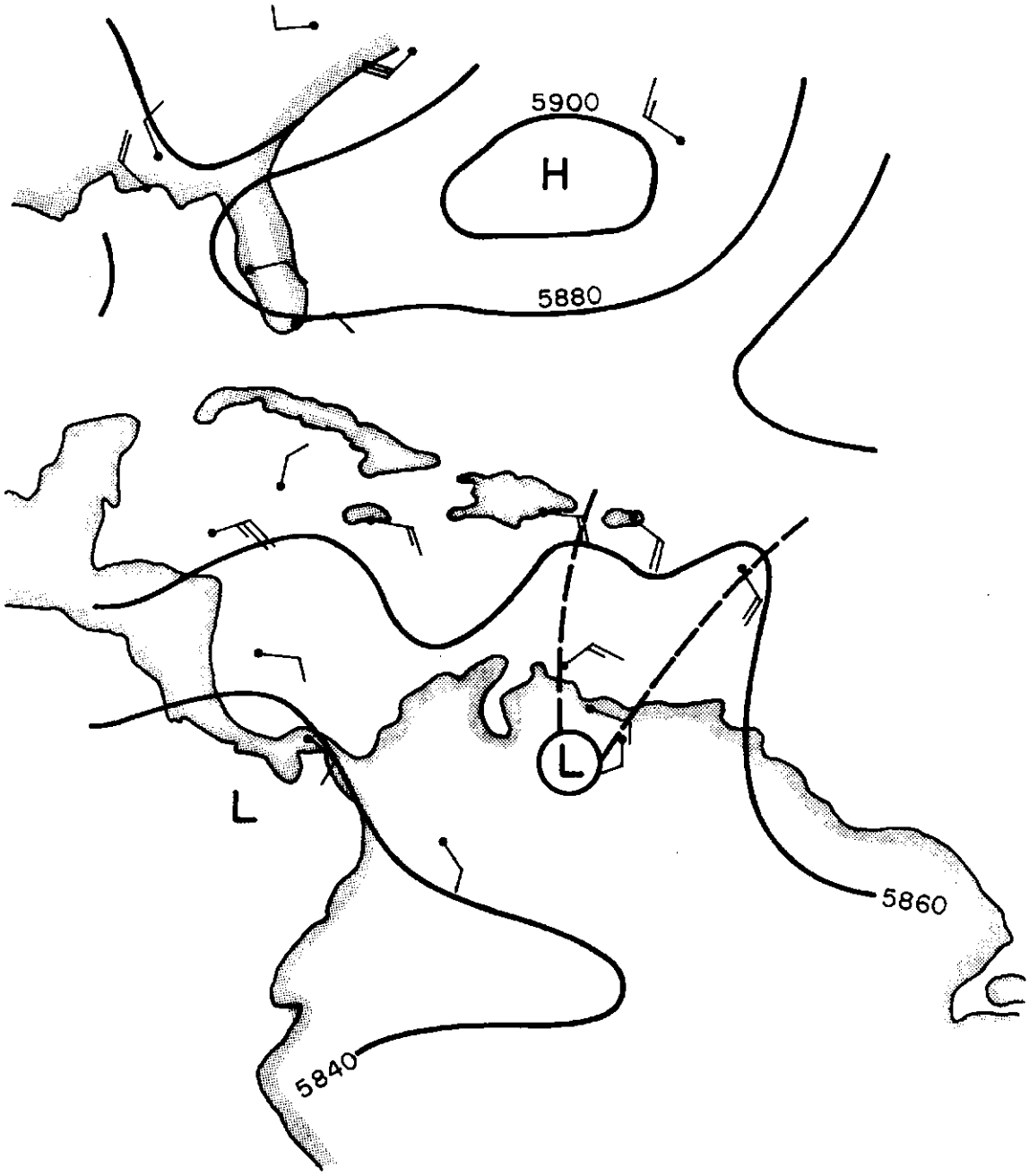

Figure 4.9 - Height pattern on 500 mb surface at 1200 Z,
September 2, 1972.

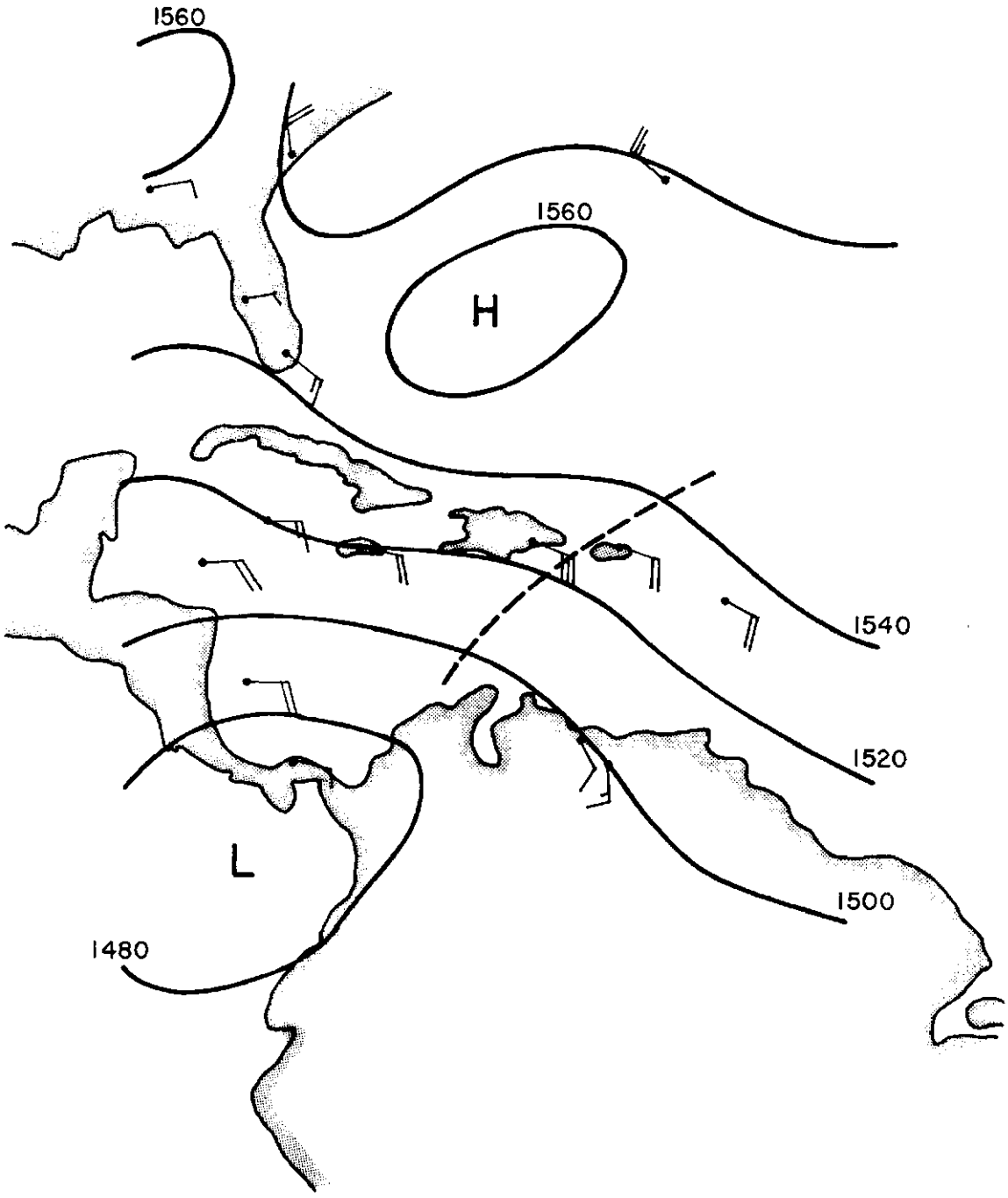

Figure 4.10 - Height pattern on 850 mb surface at 1200 2, September 2, 1972.

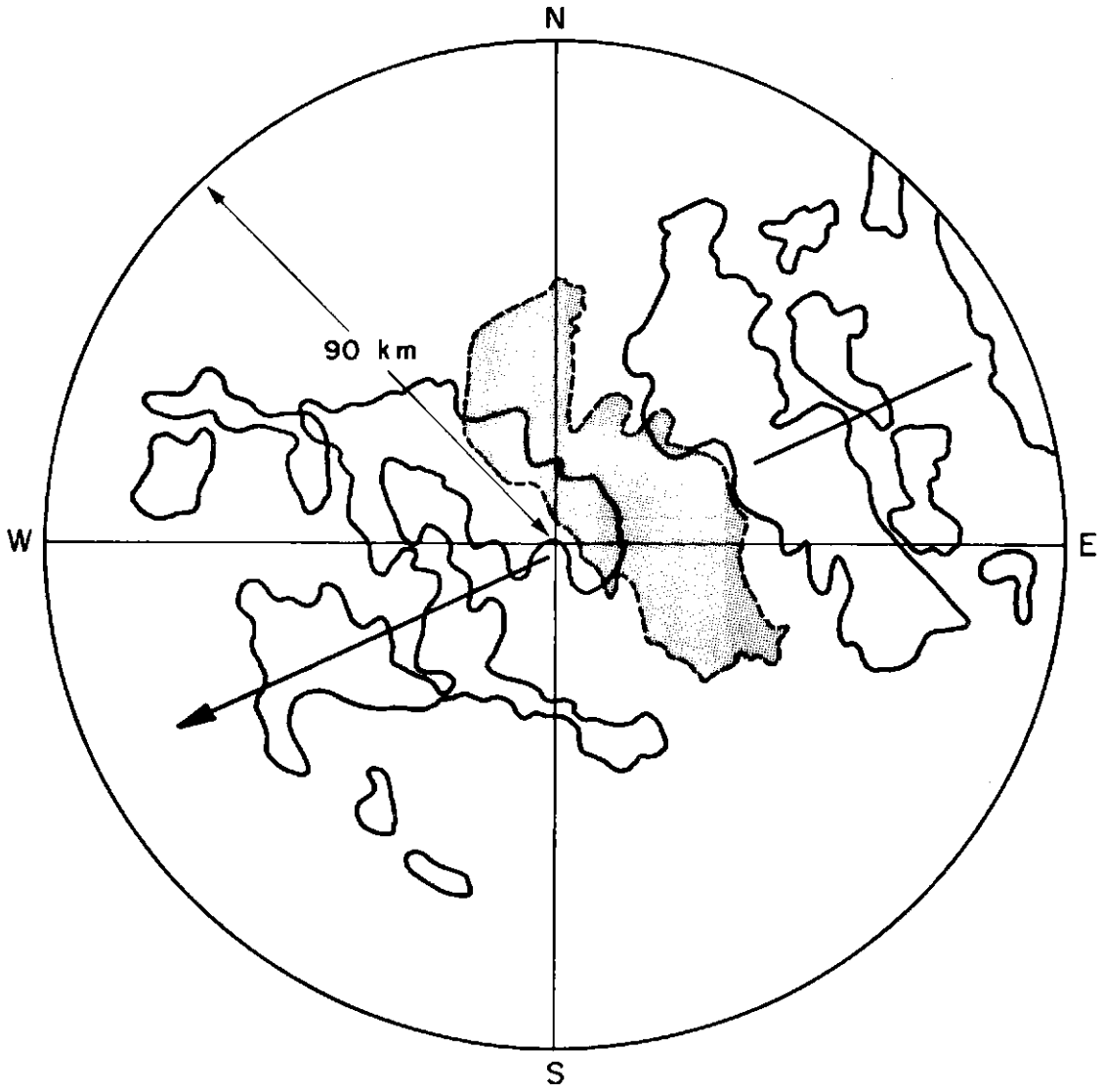

Figure 4.11 - Storm 47 at 1/2 hour intervals from 1615 LST on July 24, 1972 as seen by radar.

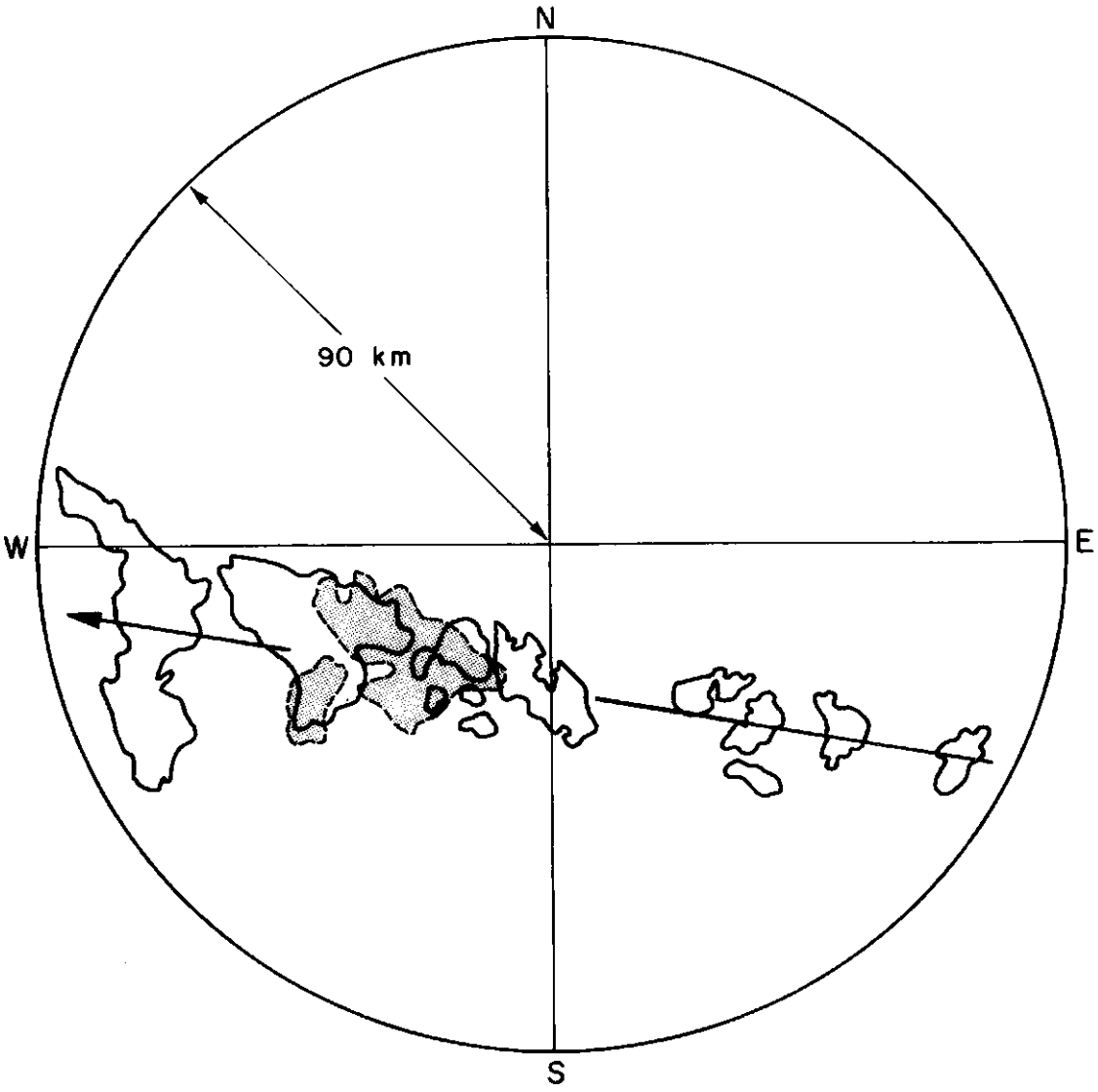

Figure 4.12 - Storm 68 at 1/2 hour intervals from 1400 LST on August 12, 1972 as seen by radar.

allowed the flow to be considered two dimensional within the immediate vicinity of the mid-sections of the storms. These characteristics show the strong relationship between Group 1 storms and Moncrieff's theory.

Storm 68 is shown in Figure 4.12. Here the storm is shown at half hour intervals from its initial contact at 1400 LST. This storm is the smallest of Group 2 storms and was included in the original set of fifteen because of its change of structure near the end of radar coverage.

In general, Group 2 storms tended to be less organized and smaller than those of Group 1. The line configuration was not always apparent and the storm shapes changed more readily. Thus, Group 2 storms did not correlate with the theory as well as did Group 1 storms.

4.5 Propagation Speed

The predicted propagation speeds for each group were compared with the observed propagation speeds using

$$C_0 = u_M + \alpha(Ri)(APE)^{1/2}$$

where c_0 is the observed propagation speed, u_M is read from the u_r profiles of the storm at the mid-point of the convection ±25 mb and α(Ri) is obtained from Figure 2.2. Shown in Table 4.4 are the results of calculating $.2(APE)^{1/2} - (c_0 - u_M)$. The mean and standard deviation for the subtracted values show the Group 1 storms to most closely agree with the predicted propagation speeds.

Figures 4.13 and 4.14 show the observed propagation speed plotted against the predicted propagation speed for Group 1 and Groups 2 and 3. Sample error bars of ±1 ms^{-1} have been placed on one storm in each

TABLE 4.4

Propagation Speed Evaluation

Storm Number	Ri	$.2(APE)^{1/2}$		$.2(APE)^{1/2} - (c_0-u_H)$
Group 1				
27/99	-0.93	4.6	10.0	- 5.4
60/226	-0.95	6.3	7.1	- 0.8
47/176	-1.1	5.7	7.6	- 1.9
27/100	-1.1	3.6	7.3	- 3.7
60/227	-1.5	5.5	6.2	- 0.7
35/120	-2.0	6.9	6.3	+ 0.3
91/289	-2.1	7.8	4.3	+ 3.5
91/288	-2.3	7.1	5.2	+ 1.9
64/241	-3.1	8.2	7.8	+ 0.4
Group 2				
126/169	-0.58	3.4	8.6	- 5.2
17/88	-0.59	4.6	17.5	-12.9
80/271	-0.67	3.4	10.9	- 7.5
134/235	-0.69	5.9	13.2	- 7.3
53/192	-0.76	3.5	6.4	- 2.9
16/87	-0.79	5.2	15.3	-10.1
68/245	-0.91	6.1	8.2	- 2.1
134/236	-1.3	5.0	10.6	- 5.6
53/191	-1.3	6.1	7.5	- 1.4
Group 3				
109/316	-1.7	5.4	9.0	- 3.6
108/312	-3.5	6.8	4.6	+ 2.2

Group 1	Group 2	Group 3
$\bar{\chi}$ = -.71	$\bar{\chi}$ = -6.11	$\bar{\chi}$ = -.70
S = 2.72	S = 3.79	S = 4.10

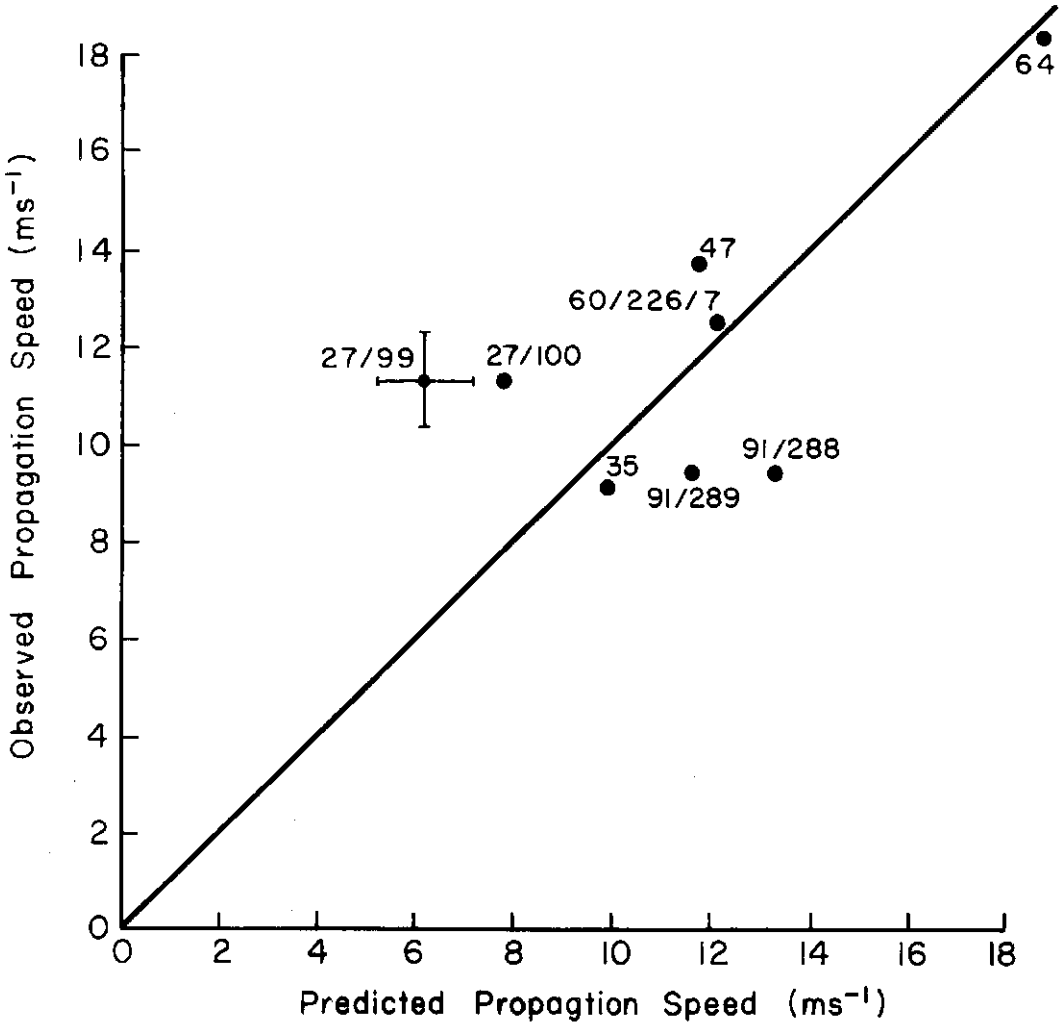

Figure 4.13 - Predicted vs. observed propagation speed for Group 1 storms.

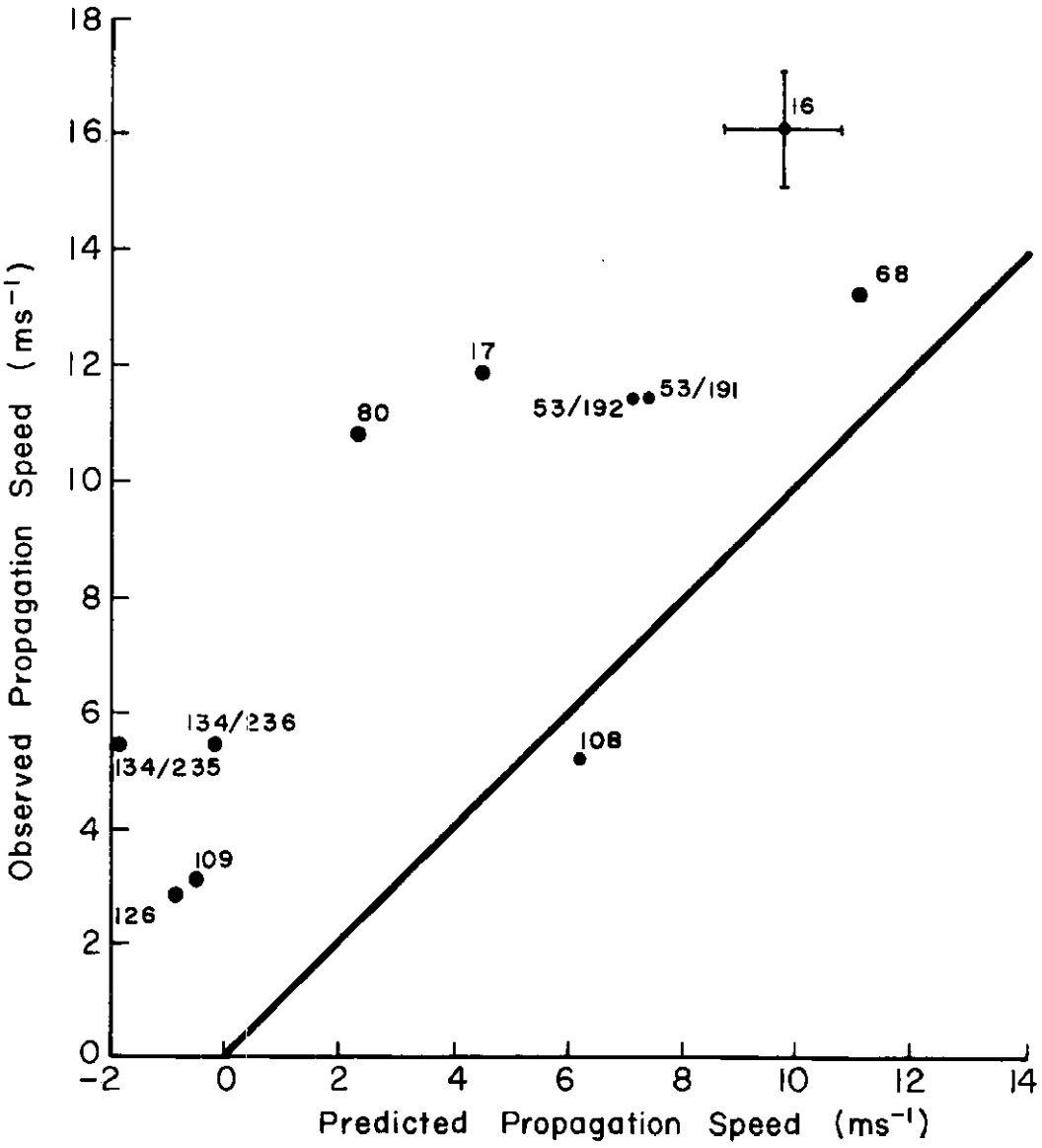

Figure 4.14 - Predicted vs. observed propagation speed for Group 2 and 3 storms.

graph. From Sections 3.3 and 3.4, the observed propagation speed had a probable error of ±1 ms^{-1} while the largest single source of error in

$$C_0 = u_M + \alpha(Ri)(APE)^{1/2}$$

is the available potential energy. The $(APE)^{1/2}$ error is dependent upon the individual storm, but probably does not exceed 10%. Other sources of error in the above equation are the variation of u_M at ±25 mb of the mid-point of the convection and the accuracy of α (Ri). On the average, u_M varied 5% while the variation α creates at most a 2% error in the predicted propagation speed.

4.6 Atmospheric Modification by Group 1 and Group 2 Storms

An analysis of the atmosphere after the passage of each group of storms shows the degree the atmosphere has been modified. In each group, storms with soundings measuring the inflow and outflow regions of the storm were selected. The inflow soundings were averaged and compared with the averaged outflow soundings at 25 mb pressure intervals, from the surface to 150 mb for θ, r, θ_e and u_r.

From Group 1, storms 35, 47, 60 and 64 had inflow/outflow soundings. These four storms fit the propagation theory well (see Figure 4.13). Figure 4.15 shows a composite squall-line drawn from the averaged major and minor axes of the four Group 1 storms. Positioned about this composite squall-line relative to individual squall-line centers are the inflow and outflow soundings. Storm 91 had only inflow coverage while the outflow sounding for Storm 27 contained errors, requiring removal of both from the average.

Figure 4.16 shows the averaged inflow/outflow profiles for θ. As expected, there is a definite cooling of the lower atmosphere, a

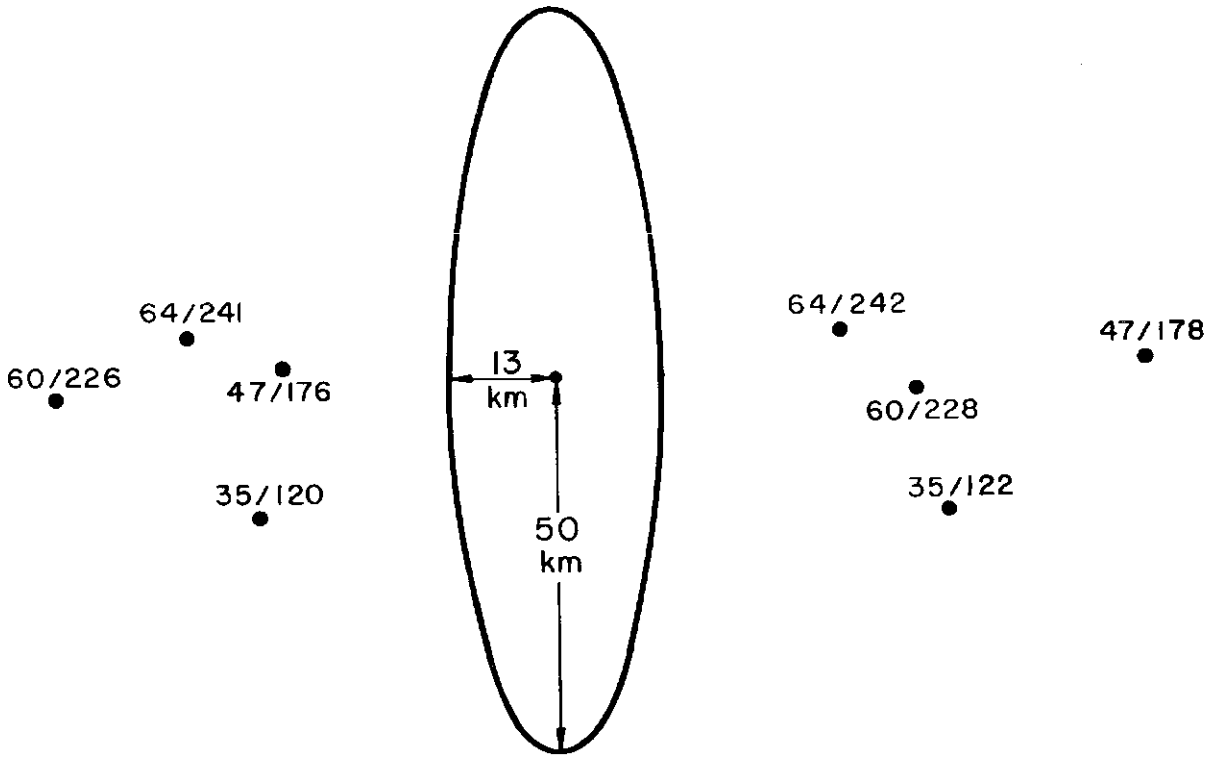

Figure 4.15 - Composite squall-line with radiosondes.

result of the downdraft. The most interesting features of these curves are (1) the warming of the layer between 825 and 650 mb and (2) the marked cooling of the layer between 650 mb and 300 mb of about 1°K. At present, the significance of these two features is not apparent. The greater cooling above 250 mb may be caused by combination of parcel overshoot (Betts, 1970) and radiative cooling.

The modification of the mixing ratio (r) structure is presented in Figure 4.17. It shows a decrease of r in the lower 330 mb of the atmosphere and an increase in r above 700 mb. The changes in these profiles, though significant, do approximately balance. There was, however, considerable rainfall from these squall-lines indicating the convergence of the moisture into the system is approximately equal to the rainfall.

Figure 4.18 shows the e_e profiles. There is a well defined fall in the lower 300 mb. This is a result of cooler, dryer air from mid- levels of the atmosphere replacing the warm moist air during the passage of the convective activity. From 700 mb to 250 mb an increase in θ_e has taken place. This reflects the so-called "hot tower" transport identified by Riehl and Malkus (1958). It is of interest to note that the transition points of both the e_e and r curves occur at 700 mb, and that the distinctive fall of θ_e beginning at 250 mb corresponds to the increased cooling of the e profiles at this level.

Shown in Figure 4.19 are the u_r profiles. Printed to the outside of each curve is the θ_e value that corresponds to the curve and pressure level. This was done in an effort to trace the levels at which the inflow air left the system by assuming the conservation of θ_e. The wind profiles show inflow into the system at all levels

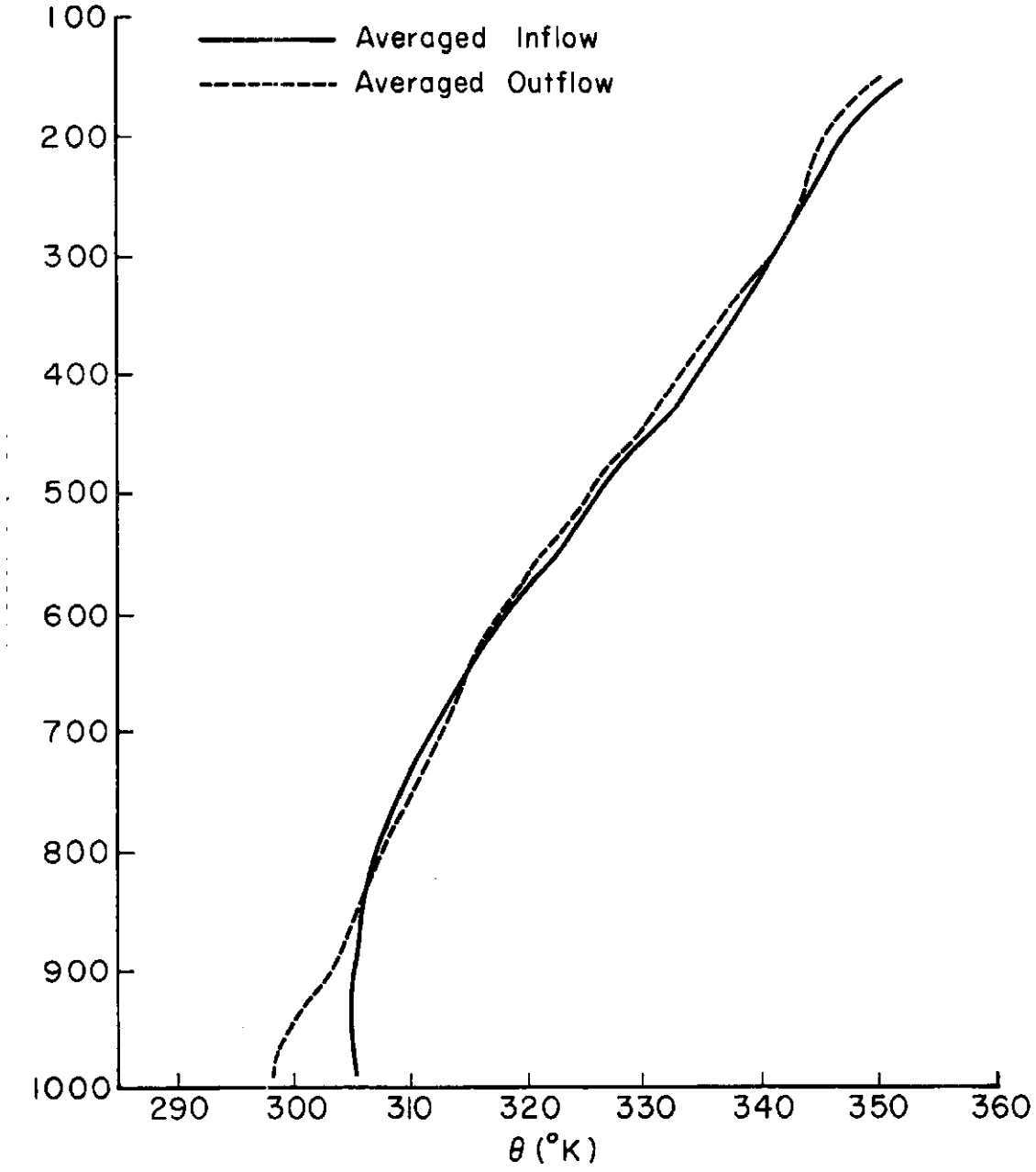

Figure 4.16 - Composite squall-line θ profiles.

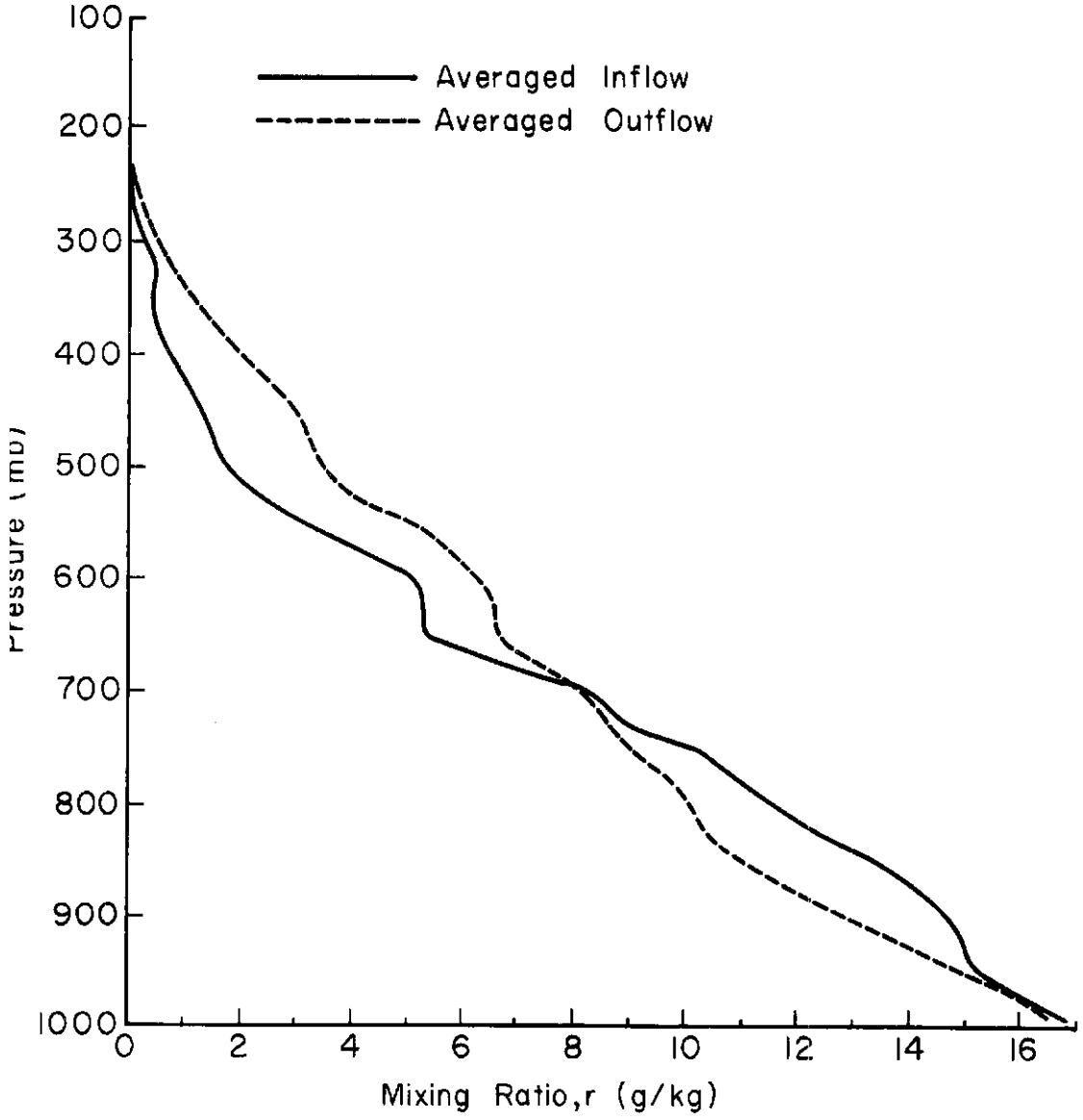

Figure 4.17 - Composite squall-line r profiles.

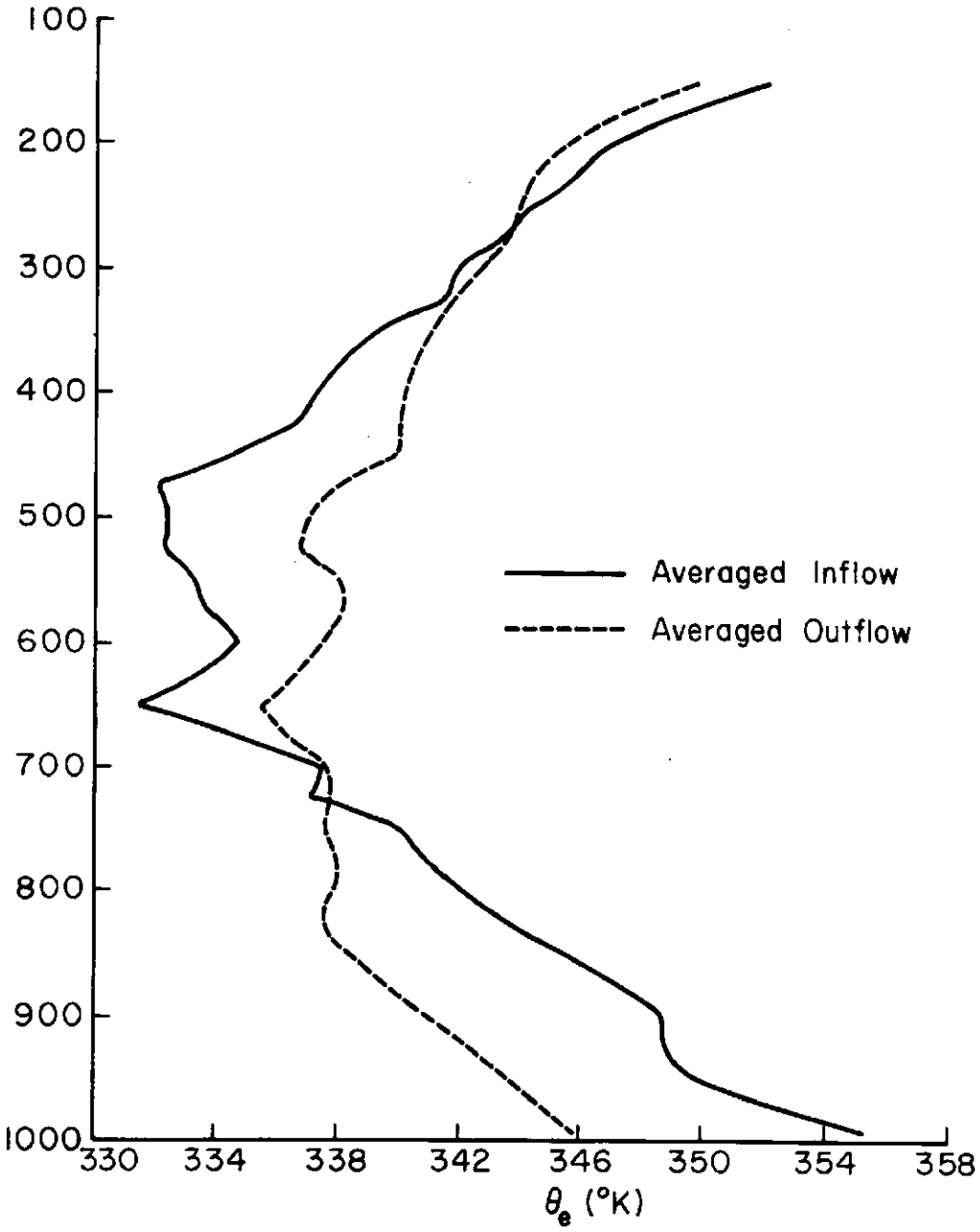

Figure 4.18 - Composite squall-line θ_e profiles.

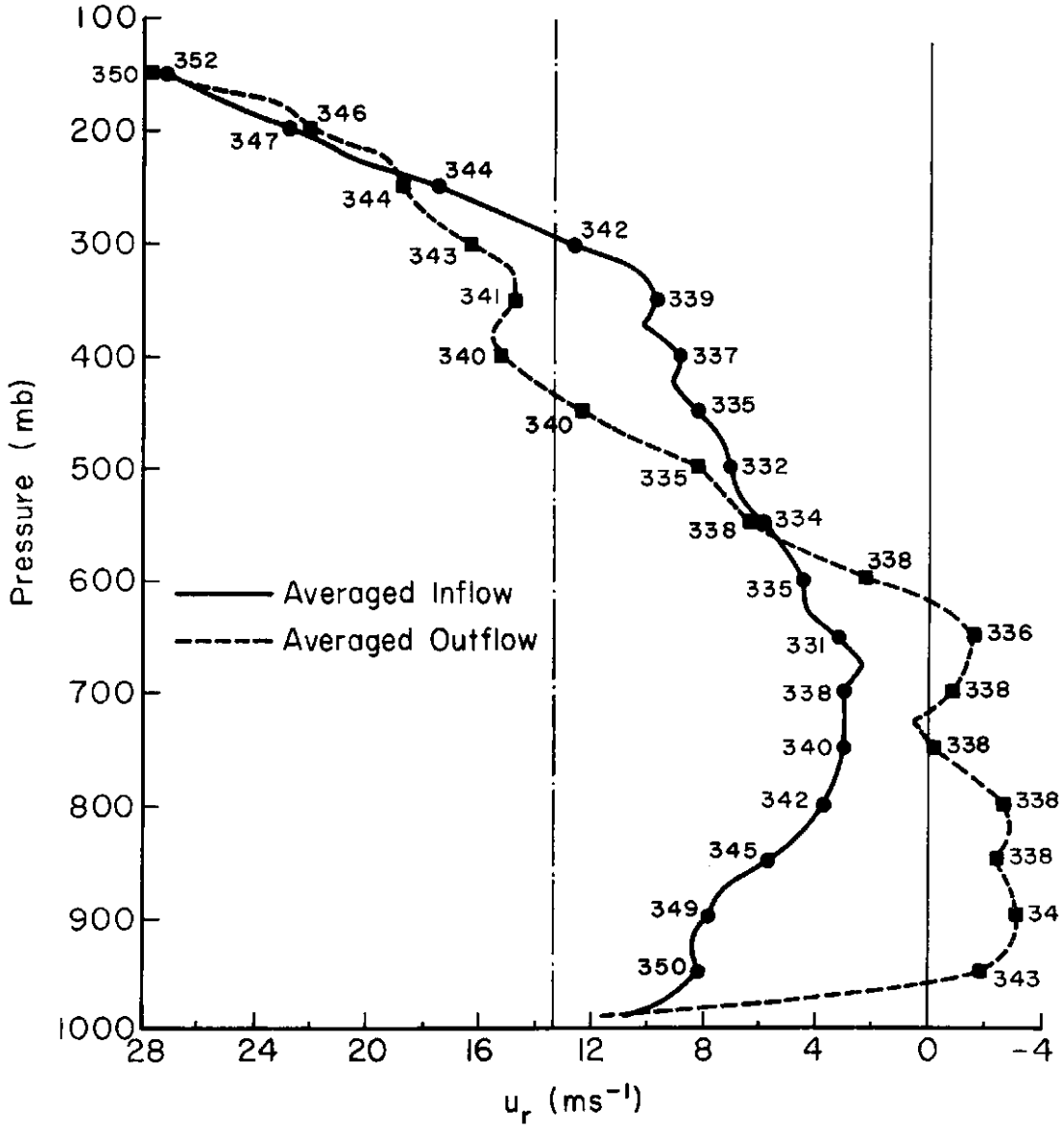

Figure 4.19 - Composite squall-line u_r profile. Shown to the outside of each curve is the θ_e value at that level.

(Section 2.2). The averaged inflow profile is different from the idealized inflow configuration of the model (Figure 2.3). The vertical line at 13.3 m/s is the average propagation speed of the four systems. The outflow profile reveals a definite change in the atmospheric wind structure. There is a large injection of easterly momentum into the lower atmosphere and a depletion of the same at the upper levels. A comparison of the two areas shows a lack of mass balance. This is attributed to the two dimensionality of the analysis. The 560 mb transition of the wind profiels corresponds exactly to the average mid-point of the convection depth.

The momentum transfer, as predicted by theory (Figure 2.4), is significantly different from what is observed (Figure 4.19). This difference is attributable to the configuration of the inflow profile used in the theory. It is suggested that the inflection point of the velocity profile be at 700 mb, rather than coincident with the midpoint of the convection. Clearly, however, more development of the theory is needed.

The e_g values that accompany the wind profile show 340 K to 350 K air entering the system from the surface to 750 mb. This air can then be found exiting in the 450 to 150 mb layer. The lowest θ_e air, 331 K to 332 K, enters the system at 650 and 500 mb. This air cannot be traced in the outflow. The lowest θ_e air in the outflow profile is found at 650 mb (336 K) and 500 mb (335 K). This fact suggests the low θ_e air entering the storm is being mixed with the updraft air and the air entering from the rear of the system. The downdraft air, seen from 750 mb to 900 mb in the outflow profile, is probably modified low

θ_e air entering the rear of the system, where it is mixed with the high θ_e updraft air and exits at the surface.

Based upon the u_r and θ_e inflow/outflow profiles, a tentative observational model of the composite system is presented in Figure 4.20. This picture represents the dynamic structure of a land tropical squall- line. Topographically, the structure in Figure 4.20 is impossible in two dimensions. However, this picture serves as a means for gaining an intuitive understanding of the dynamic structure of a squall-line. Entering the front of the system at the surface is the high θ_e air that rises through the system, leaving at the higher levels to the rear. During the ascent, the moisture contained in this air condenses and falls out as water, perpetuating the downdraft. The slant of the updraft enables the precipitation to fall out without interfering with the updraft. The updraft air exiting the rear of the system above 500 mb is probably responsible for the increased momentum observed in Figure 4.19.

There are two potential source regions for the downdraft. The first is air entering the front of the system between 700 mb and 500 mb. This air encounters the inflow air from the rear of the squall-line and is moved downward into the downdraft. The second region is the air flowing into the rear of the squall-line between 800 mb and 700 mb. It is suggested that the air around 700 mb might encounter the air flowing from the front of the system and be forced upward, while the air at 900 mb to 800 mb could move downward to pass out of the squall-line to the rear. As this downdraft air reaches the surface it spreads forward, enhancing the lifting action of the updraft and creating the cool down rush felt prior to the onset of precipitation.

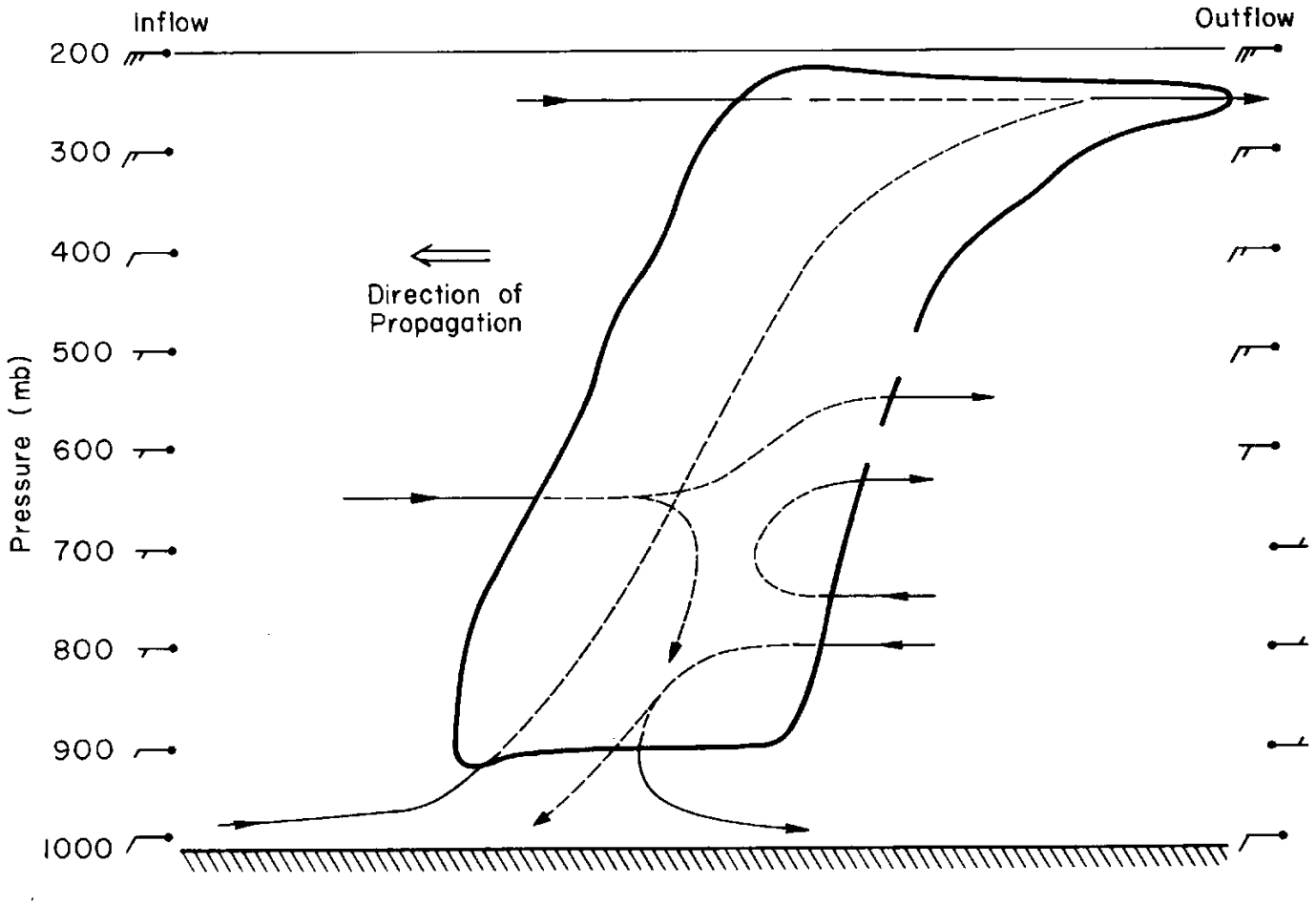

Figure 4.20 - Proposed dynamic structure of a land tropical squall-line.

The tentative observational model differs from the cumulonimbus model proposed by Moncrieff (Figure 2.1). The updraft configuration of the two models do agree. However, Moncrieff's proposed downdraft is not satisfactory. From the results presented in this section, it appears that the air entering the upper levels of the squall-line passes through the system and leaves at or near the same level at which it enters. Moncrieff did not allow for the possibility of low level inflow into the rear of the squall-line. This fact has the potential of altering the theoretical model. However, in general the observations do support the model's concept of a complete dynamic and thermodynamic overturning of the atmosphere.

When comparing the averaged inflow/outflow profiles of Group 1 with the averaged profiles of Group 2, it should be apparent that they represent different dynamic structures. The results of averaging inflow/ outflow soundings for Group 2 storms 16, 17 and 68 (the remainder of Group 2 storms only had inflow soundings) are markedly different from those of Group 1. The position of the inflow and outflow soundings about the composite Group 2 system is shown in Figure 4.21.

Shown in Figure 4.22 are the e profiles. The profiles show the cooling at the surface as experienced by the Group 1 composite. However, above 850 mb there is virtually no difference in the profiles until 200 mb, where the outflow is cooler than the inflow. Even though this cooling is observed, it is far from the magnitude of that displayed by the composite squall-line.

Figure 4.23 shows the r profiles. The interesting feature of these two curves is the atmosphere's increased moisture content. This

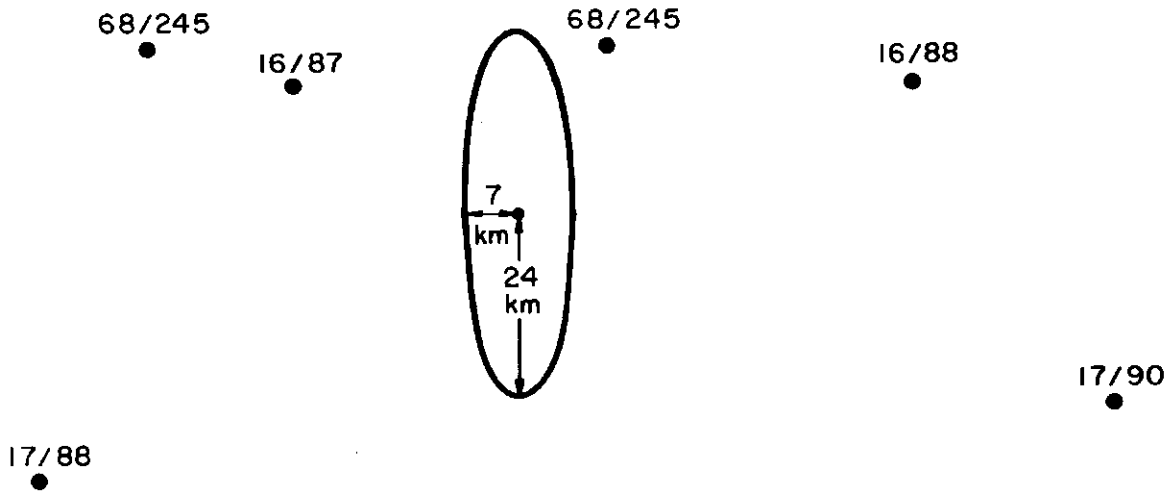

Figure 4.21 - Composite non-squall-1ine with radiosondes.

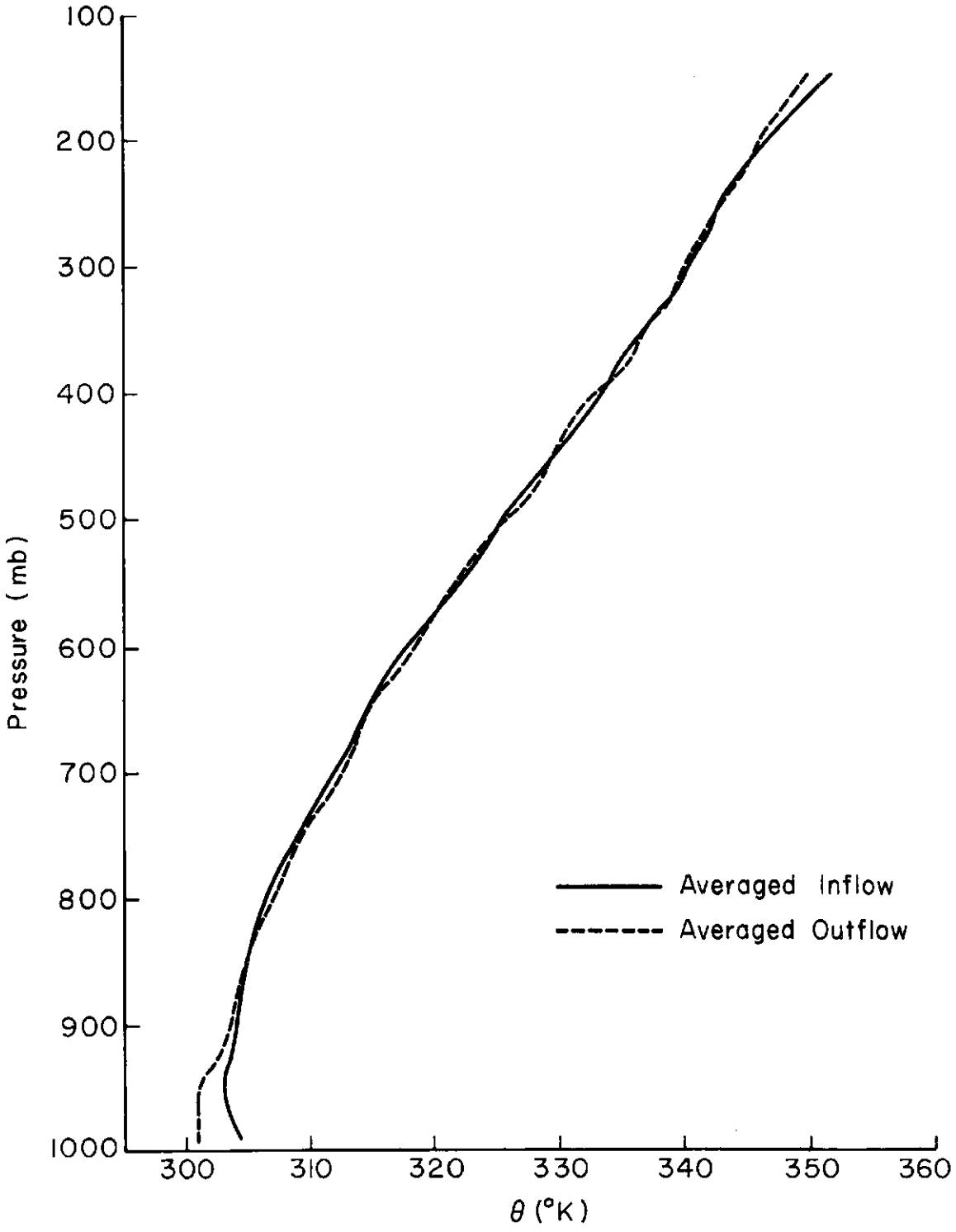

Figure 4.22 - Composite non-squall-1ine e profiles.

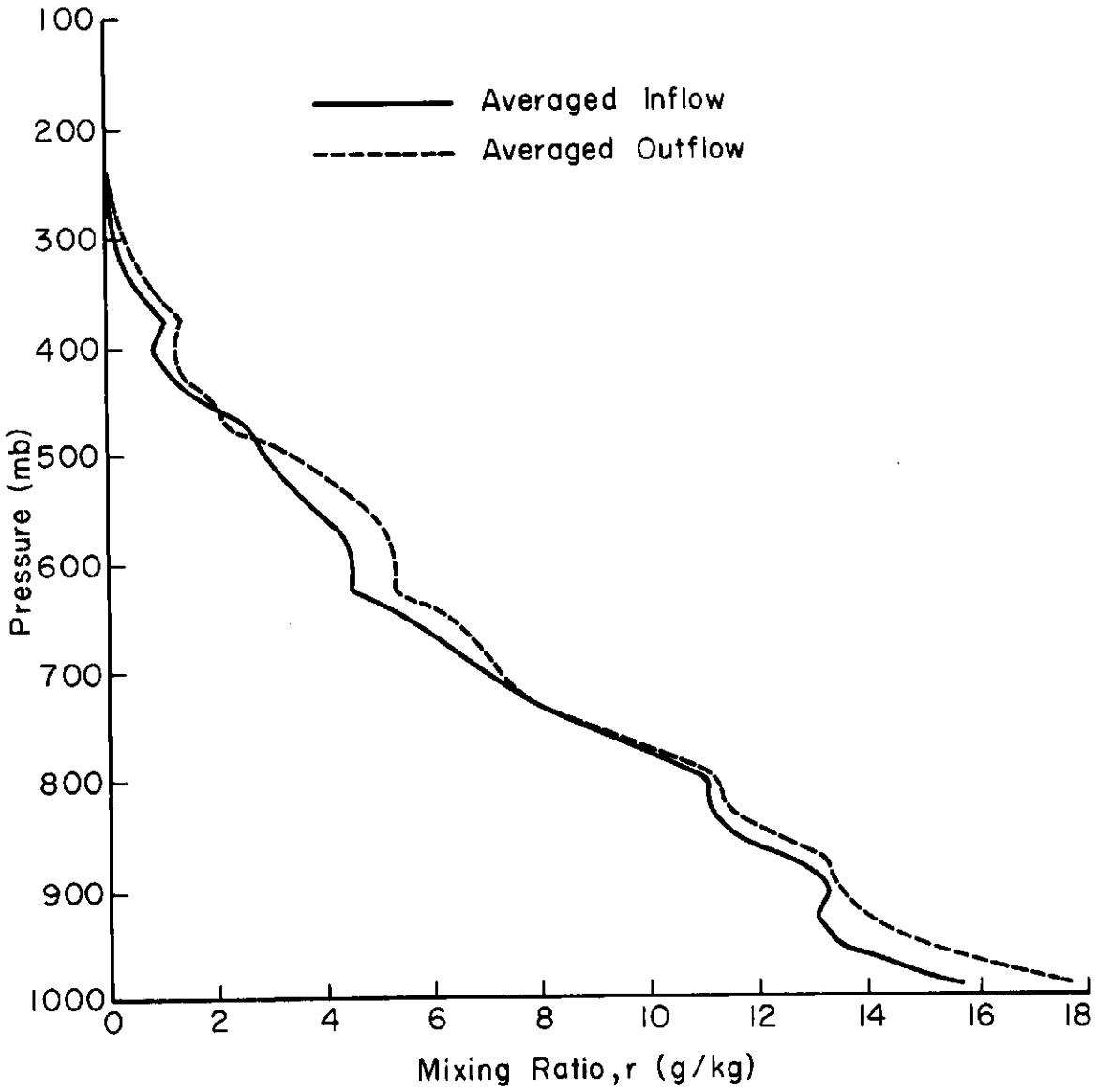

Figure 4.23 - Composite non-squall-line r profiles.

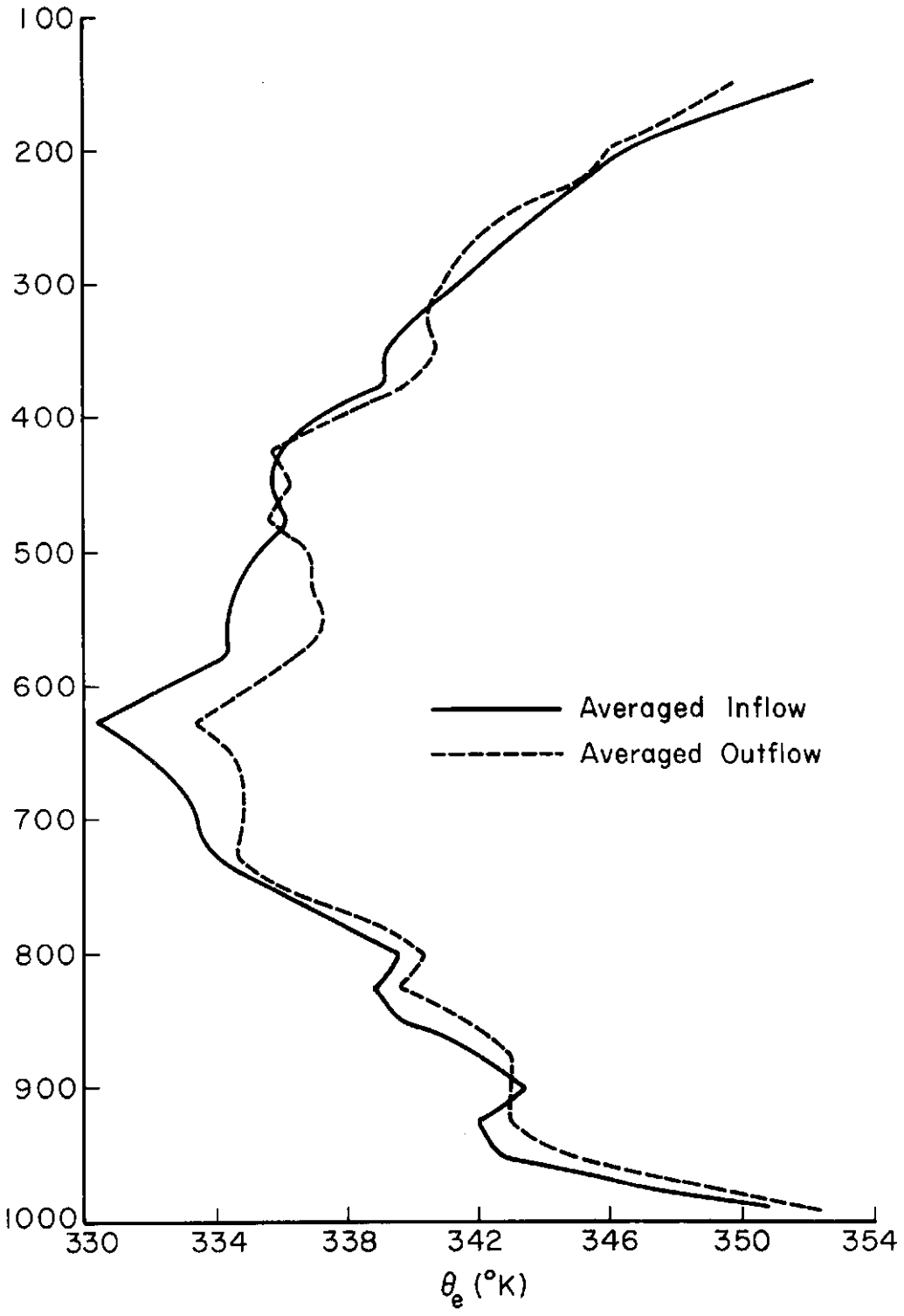

Figure 4.24 - Composite non-squall-line θ_e profiles.

5. SUMMARY AND CONCLUSIONS

Fifteen storm systems were selected from the VIMHEX II storm data by applying assumptions of Moncrieff's cumulonimbus and squall-line model (1974a). Analysis of the Richardson Number, synoptic features, geometric and dynamic characteristics and propagation speeds for the fifteen storms resulted in the indentification of three groups: squall-lines, non- squall -lines and large, non-propagating mesosystems.

The Richardson Numbers for the squall-lines were ≤ -0.93, while those for the non-squall-lines were between -0.91 and -0.58. Analysis of squall- line synoptic conditions showed an 850 mb trough coincident with the occurrence of four out of six squall-lines, suggesting its presence may be a triggering mechanism for the squall-lines. The 850 mb trough was absent in the non-squall-line cases. The size and organization of the squall-lines correlated with the assumptions of two dimensionality and steady state of Moncrieff's model. Correlation of theory with the non- squall-line systems was complicated by their being smaller and less organized. Moncrieff's theoretical propagation speed was found to be more applicable to the squall-lines than to non-squall-lines.

The mesosystems were shown to have the squall-line features of the 850 mb trough and organization. However, their configuration and size were unique among the fifteen storms and they lacked propagation speed. There were only two storms in this category, both lacking outflow sounding data. Thus, they were not analyzed further.

Composite structures of the unmodified and modified atmosphere were drawn from averaged inflow and outflow soundings for the squall-lines and

non-squall-lines. The squall-line composite showed the atmosphere to have undergone a significant change at all levels. The observed modified wind profile (Figure 4.19) differs from that predicted by Moncrieff (Figure 2.3). This difference is in part attributable to the difference in configuration of the inflow profiles (Figures 2.3 and 4.19).

An observational model was proposed (Figure 4.20). The updraft configuration compares with Moncrieff's model (Figure 2.1). However, the inflow trajectories at the upper levels and the origin of the down- draft differ significantly. The difference can be atrributed to the simplicity of the theoretical model.

The inflow/outflow soundings are averaged for three non-squall-line systems. The results indicate a storm structure quite different from the proposed dynamic squall-line structure. The small sample size prevented the construction of an observational model.

The land tropical squall-lines analyzed herein compares favorably to Moncrieff's cumulonimbus and squall-line model. The results from analysis of squall-line and non-squall-line systems suggest the model as originally proposed may not be applicable to the general class of tropical cumulonimbus convection.

REFERENCES

Arakawa, A., and W. H. Schubert, 1974: Interaction of a Cumulus Cloud Ensemble with the Large Scale Environment. Part I., J. Atmos. Sci., 31, pp. 674-701.

Atlas, D., 1973: Personal Communication to Dr. A. K. Betts.

Betts, A. K., 1970: Cumulus Convection. Unpublished Ph.D. thesis. Imperial College of London, 151 pages.

Betts, A. K., 1973a: Non-Precipitation Cumulus Convection and Its Parameterization. Quart. J. Roy. Meteor. Soc., 99, pp. 178-196.

Betts, A. K., 1973b: A Composite Mesoscale Cumulonimbus Budget. J. Atmos. Sci., 30, pp. 597-610.

Betts, A. K., 1973c: Precalibration of VIZ-NWS Radiosonde. Bull. Amer. Meteor. Soc., 54, pp. 222-223.

Betts, A. K., F. J. Dugan and R.W. Grover, 1974: Residual Errors of the VIZ Radiosonde Hygristor as Deduced from Observations of Subcloud Layer Structure. Submitted to Bull. Amer. Meteor. Soc.

Dugan, F. J., 1973: The Thermodynamic Structure of the Cumulus Sub-Cloud Layer. Atmospheric Science Paper No. 205, Department of Atmospheric Science, Colorado State University, 97 pages.

Joint Organizing Committee, GARP, 1970: Report on the First Session of the J0C Study Group on Tropical Disturbances, 1968. Appendix 1, GARP Publication Series No. 4.

Malkus, J. S. and H. Riehl, 1964: Cloud Structure and Distributions Over the Tropical Pacific Ocean. Tell us, 16., pp. 275-287.

Mielke, P. W. Jr., 1974: Personal Communication.

Moncrieff, M. W., 1972: Advanced Dynamics - Lecture Notes. Imperial College of London, Unpublished manuscript, 53 pages.

Moncrieff, M. W., 1973: Structure and Regimes of Convection. Unpublished manuscript, 21 pages.

Moncrieff, M. W., 1974a: The Dynamics of Tropical Cumulonimbus and Squall-Lines. Unpublished manuscript, 24 pages.

Moncrieff, M. W., 1974b: Personal Communication.

Moncrieff, M. W., and J. S. A. Green, 1972: The Propagation and Transfer Properties of Steady Convective Overturning in Shear. Quart. J. Ro.y. Meteor. Soc., 98, pp. 336-352.

REFERENCES - Continued

Riehl, H. and J. S. Malkus, 1958: On the Heat Balance of the Equitorial Trough. Geophysica,6, pp. 503-538.

Riehl, H. and A. K. Betts, 1972: Humidity Observations with the 1972 U. S. Radiosonde Instrument. Bull. Amer. Meteor. Soc., 53, pp. 887-888.

BIBLIOGRAPHIC DATA SHEET	1. Report No. CSU-ATSP-228	2.	3. Recipient's Accession No.
4. Title and Subtitle Characteristics of Tropical Squall-Lines Over Venezuela			5. Report Date July 1974 6.
7. Author(s) Ralph W. Grover			8. Performing Organization Rept. No. CSU-ATSP-228
9. Performing Organization Name and Address Department of Atmospheric Science Foothills Campus Colorado State University Fort Collins, Colorado 80523			10. Project/Task/Work Unit No. 11. Contract/Grant No. NSF GA-33182 P. I. - A. K. Betts
12. Sponsoring Organization Name and Address Atmospheric Sciences Section National Science Foundation Washington, D. C. 20550			13. Type of Report & Period Covered M.S. Thesis 14.

15. Supplementary Notes

16. Abstracts — The characteristics of fifteen mesoscale storm systems observed during the 1972 Venezuelan International Meteorological and Hydrological Experiment were compared with the predictions of a dynamic cumulonimbus and squall-line model proposed by Moncrieff (1974a). The fifteen systems seemed to fall into three groups: one group of six were land tropical squall-lines; a second group of seven are simply called non-squall-lines; and the third group of two storms formed a distinct class which are here called large non-propagating mesosystems. Moncrieff's theoretical model, which predicts storm propagation speeds, is applied to each group, and closest agreement is found with the group of squall-lines. A simple composite of the inflow and outflow environments of the squall-lines is presented. This shows the complete dynamic and thermodynamic transformation of the atmosphere, which, as predicted by the theory, results from the passage of a squall-line. A schematic model for a squall-line is presented from this composite. It suggests that although the observed updraft configuration may be similar to that of the theoretical model, the observed downdraft is more complex.

17. Key Words and Document Analysis. 17a. Descriptors

Tropical Squall-lines

Dynamics of Convection

Cumulonimbus Convection

Atmospheric Structure

17b. Identifiers/Open-Ended Terms

17c. COSATI Field/Group

18. Availability Statement	19. Security Class (This Report) UNCLASSIFIED	21. No. of Pages 79
	20. Security Class (This Page UNCLASSIFIED	22. Price